Burns & Trauma, 2026, **14**, tkaf076
https://doi.org/10.1093/burnst/tkaf076
Advance access publication date 24 November 2025
Research Article

Multi-enzyme active temperature-sensitive hydrogel with reactive oxygen species scavenging and antimicrobial capacity for diabetic wound repair

Wenxuan Fan[1,‡], Ji Cheng[1,‡], Yonghai Wang[2], Hanjing Lu[2], Jiacheng Li[1], Hanbin Deng[1], Xingxin Guo[1], Huwen Wu[1], Peishen Zhang[1], Han Zhou[1], Ding Luo[2], Zuojia Guo[2], Jinghua Li[1,*], Shaowen Cheng[1,*]

[1]Key Laboratory of Emergency and Trauma of Ministry of Education, Key Laboratory of Hainan Trauma and Disaster Rescue, Department of Wound Repair, The First Affiliated Hospital, Hainan Medical University. No. 31 Longhua Road, Longhua District, Haikou, Hainan 570105, China
[2]Emergency Department, The First Affiliated Hospital, Hainan Medical University. No. 31 Longhua Road, Longhua District, Haikou, Hainan 570105, China

*Corresponding authors. Jinghua Li, E-mail: anubiss1860@163.com; Shaowen Cheng, E-mail: chengshaowen1@126.com

‡These authors contributed equally to this work.

Abstract

Background: Diabetic wound healing is often impaired due to the high-glucose microenvironment in patients. Among the relevant factors, bacterial infection and overproduction of reactive oxygen species (ROS) have critical roles, and sustained oxidative stress further impairs angiogenesis and increases apoptosis, thereby hindering wound repair. To reduce these effects, we aimed to develop an injectable temperature-sensitive cellulose hydrogel exhibiting anti-apoptotic, oxidative stress-attenuating, antimicrobial, and multi-species enzymatic activities.
Methods: By simulating the dual active sites of natural copper–zinc superoxide dismutase (CuZn–SOD), a bimetallic mimetic nanoenzyme [Cu/Zn-metal–organic framework (MOF)] was synthesized. Subsequently, Cu/Zn-MOF was incorporated into a hydroxypropyl methylcellulose hydrogel, and the gelation temperature was adjusted to enable a sol-to-gel transition near physiological temperature. A rheometer was used to measure the gelation temperature, and scanning electron microscopy was performed to characterize the surface morphology. The hydrogels were evaluated for multiple enzyme-like activities, including those of SOD, glutathione peroxidase (GPx), thiol peroxidase (TPx), and ascorbate peroxidase (APx). Mouse fibroblasts (L929 cells) and human umbilical vein endothelial cells were used to assess antioxidant, pro-migratory, pro-angiogenic, and anti-apoptotic properties. Antimicrobial activity was assessed against *Escherichia coli* and *Staphylococcus aureus*. Western blotting was performed to verify potential anti-inflammatory mechanisms. Finally, wound and infected-wound models were established in diabetic mice to evaluate the hydrogel's effects on wound repair.
Results: The hydrogel exhibited a sol-to-gel transition at 37°C and demonstrated favorable injectability and hydrophilicity, providing a moist healing environment. The Cu/Zn-MOF nanoenzymes demonstrated four enzyme-like activities (SOD, GPx, TPx, and APx), enabling cascade ROS scavenging, which was further confirmed in cellular experiments. The Cu/Zn-MOF nanoenzymes also modulated Sirt1/nuclear factor-κ beta expression to influence inflammatory factor release, thereby exhibiting strong anti-inflammatory activity. The hydrogel also exerted cell migration, angiogenesis, and anti-apoptotic effects. Antimicrobial assays showed kill rates of 99.39% and 99.67% against *Escherichia coli (E. coli)* and *Staphylococcus aureus (S. aureus)*, respectively. In a diabetic mouse wound model, the hydrogel significantly enhanced pro-healing effects by promoting neovascularization and collagen deposition through ROS and bacterial clearance, thereby reducing the inflammatory response.
Conclusions: Biomimetic nanoenzymes were synthesized and incorporated into temperature-sensitive injectable hydrogels, which exhibited strong antioxidant and antimicrobial activities that have considerable potential for diabetic wound therapy.

Keywords: Diabetic wounds; Bionic nanoenzymes; Temperature-sensitive hydrogels; Reactive oxygen species; Angiogenesis; Antimicrobial

Highlights

- To simulate the ligand characteristics of natural enzymes, a biomimetic bimetallic nanoenzyme Cu/Zn-MOF was synthesized to enhance enzyme-like activity.
- Temperature-sensitive injectable hydrogels (termed HCG@Cu/Zn-MOF) were fabricated by using the thermo-responsive behavior of hydroxypropyl methylcellulose, and salt ions, chitosan, and glycerol were added to achieve gelation near physiological temperature while dispersing the nanoenzymes within the matrix.
- The HCG@Cu/Zn-MOF hydrogel displayed multiple antioxidant enzyme-like activities, efficiently scavenged reactive oxygen species (ROS), provided antimicrobial effects, protected cells from oxidative stress, reduced inflammatory responses, and promoted angiogenesis and cell migration.
- The hydrogel maintained mitochondrial membrane potential stability and attenuated apoptosis.
- *In vivo*, the hydrogel scavenged ROS, showed antimicrobial effects, enhanced angiogenesis and collagen deposition, and accelerated diabetic wound healing.

Received: May 6, 2025. **Revised:** October 26, 2025. **Accepted:** November 19, 2025
© The Author(s) 2025. Published by Oxford University Press.
This is an Open Access article distributed under the terms of the Creative Commons Attribution-NonCommercial License (https://creativecommons.org/licenses/by-nc/4.0/), which permits non-commercial re-use, distribution, and reproduction in any medium, provided the original work is properly cited. For commercial re-use, please contact reprints@oup.com for reprints and translation rights for reprints. All other permissions can be obtained through our RightsLink service via the Permissions link on the article page on our site—for further information please contact journals.permissions@oup.com.

Downloaded from academic.oup.com/burnstrauma/article/doi/10.1093/burnst/tkaf076/8341464 by guest on 12 October 2026

Background

Skin has a strong barrier function, which impedes wound recovery when extensive damage occurs due to diseases, such as diabetes [1, 2]. Diabetic wounds exhibit complex pathogenesis, prolonged healing duration, and treatment challenges, thereby significantly reducing patients' quality of life [3]. These wounds often remain in a prolonged inflammatory state, characterized by a reactive oxygen species (ROS)-mediated imbalance of redox homeostasis that results in oxidative stress injury [4, 5]. Excessive ROS not only induces cellular dysfunction but also inhibits essential repair processes, including angiogenesis, granulation-tissue formation, and collagen deposition [6, 7]. Furthermore, elevated ROS aggravates mitochondrial dysfunction by decreasing mitochondrial membrane potential ($\Delta\Psi m$), altering respiratory complexes, releasing cytochrome c, downregulating transcription factor A, and increasing mitochondrial deoxyribonucleic acid fragmentation, all of which exacerbate apoptosis [8–11]. The distinct high-glycemic microenvironment of diabetic wounds provides abundant nutrients for bacterial growth, whereas vascular and neurological impairments further deteriorate the wound environment and promote ulcer formation, thereby facilitating bacterial colonization. *Escherichia coli* (*E. coli*) and *Staphylococcus aureus* (*S. aureus*) are the most common bacteria among these pathogens. Wound infections elicit excessive and persistent inflammatory responses, promote biofilm formation, and cause further vascular damage, thereby hindering wound healing [12]. Current diabetic wound treatments, including antibiotics, pharmacological agents, local debridement, and wound dressings, remain suboptimal and carry high risks of disability and recurrence [13]. To address these major challenges, diabetic wound therapy requires a multifunctional approach capable of attenuating oxidative stress to simultaneously achieve anti-inflammatory and anti-apoptotic effects as well as provide efficient antimicrobial activity, stimulating angiogenesis and epithelial regeneration, and accelerating wound healing.

Antioxidant enzymes in organisms have a crucial role in scavenging ROS [14–17]. A representative example is copper–zinc superoxide dismutase (CuZn–SOD), which exhibits notable antioxidant activity and depends on the histidine-bridged Cu–Zn structure [18]. The coordination and synergistic interactions between Cu and Zn are essential for enzymatic function. However, the enzymes secreted in diabetic wounds are insufficient to effectively mitigate oxidative stress. Consequently, catalysts with antioxidant enzyme-like properties can be used to achieve remodeling of redox homeostasis in diabetic wounds. Various nanoenzymatic therapies have been developed, including antioxidant nanoenzymatic therapy and combined antioxidant–pro-oxidant approaches. Although effective, nanoenzyme-based therapies are strongly influenced by the functional diversity and synergistic characteristics of nanoenzymes. In contrast, multi-enzymatically active nanoenzymes can simultaneously address the dual challenges of antioxidant and antimicrobial activity, thereby forming an efficient cascade system to fulfill multifaceted therapeutic requirements [19]. Previous reports have shown that nanoenzymatic catalysts demonstrated strong potential in catalytic medicine [20–22].

Unlike natural enzymes, nanoenzymes are highly efficient, easy to synthesize, and remarkably durable. Their catalytic activity can be tailored by structural modifications, enabling applications across diverse industries [23–26]. To date, >1200 nanoenzymes have been developed, including peroxidase (POD)-, oxidase-, catalase (CAT)-, SOD-, and hydrolase-like types, demonstrating a broad range of potential applications [27]. Among these, metal–organic frameworks (MOFs) bridge the gap with natural enzymes owing to their distinct porous structures, large specific surface areas, and uniformly distributed active sites and have been widely utilized in nanoenzyme development [28, 29]. Furthermore, MOFs incorporating ions, including Fe, Ce, and Zr, reportedly exhibit enzyme-mimetic properties [30, 31]. Polymetallic MOFs have also emerged as highly promising candidates for nanoenzymatic applications, and their multiple active sites enhance catalytic performance and optimize Fenton or Fenton-like reactions. For example, Mo doping enhances the POD-like activity of Cu-2-MI MOFs [32]. Similarly, Fe–Ni bimetallic MOFs possess POD-like activity and have been used in glucose sensing [33]. Therefore, in the present study, a Zn-coordinated zeolitic imidazolate framework (ZIF) was used to synthesize ZIF-8 nanoparticles that were then doped with Cu ions. Considering the coordination characteristics of natural CuZn–SOD and the advantages of MOF nanoenzymes, Cu/Zn-MOF nanoenzymes with bimetallic biomimetic sites were designed and are expected to exhibit excellent POD-like activity and be applied in diabetic wound repair.

Hydrogels, due to their three-dimensional porous structure, have been widely used as wound dressings because they retain moisture, mimic the physicochemical characteristics of the extracellular matrix to support cellular functions, and serve as carriers for local drug delivery [34, 35].Temperature-sensitive injectable hydrogels have received much interest for use in medical and minimally invasive injections. These hydrogels exhibit a reversible sol–gel transition, allowing them to conform to irregular wound surfaces [36]. Cellulose, the most abundant renewable resource, is a naturally occurring polysaccharide [37]. Various cellulose derivatives have been applied in biomedical fields, including methylcellulose (MC) hydrogels for burn-wound repair [38] and oxidized carboxymethylcellulose hydrogels for hemostasis [39]. Hydroxypropyl methylcellulose (HPMC), a derivative of MC, exhibits strong water retention, high thickening ability, good pH stability, strong adhesion, and excellent biosafety. Moreover, HPMC has demonstrated potential as a thermosensitive hydrogel dressing due to its temperature-dependent gelation behavior, transforming into a sol at low temperatures and a gel at higher temperatures [40]. Therefore, temperature-sensitive HPMC hydrogels loaded with Cu/Zn-MOF nanoenzymes can offer multiple functions, including conforming to irregular wounds, providing antioxidant effects, and promoting angiogenesis, representing a promising approach for diabetic wound repair.

This study aimed to synthesize bimetallic biomimetic nanoenzymes (Cu/Zn-MOF) to improve on the often poor diabetic wound healing capabilities of currently available treatments. Concurrently, chitosan (CS) and glycerol (GLY) were added to the HPMC solution to create a heat-sensitive HPMC/CS/GLY hydrogel with a sol-to-gel transition temperature near body temperature (also known as HCG gel). Following the incorporation of Cu/Zn-MOF nanoparticles, the hydrogel was designated HCG@Cu/Zn-MOF and applied to diabetic wounds (Figure 1). The hydrogel demonstrated

Downloaded from academic.oup.com/burnstrauma/article/doi/10.1093/burnst/tkaf076/8341464 by guest on 12 October 2026

excellent injectability and multiple antioxidant enzyme-like activities, enabling the decomposition of superoxide anions (O_2^-) and hydrogen peroxide (H_2O_2), thereby protecting cells from ROS-induced damage and attenuating inflammatory responses. The hydrogel also maintained mitochondrial membrane potential stability and exerted anti-apoptotic effects. Furthermore, the hydrogel demonstrated strong antimicrobial properties, attributed to the release of Cu and Zn ions. In a full-thickness wound model in diabetic mice, it enhanced angiogenesis and promoted wound healing by scavenging excess ROS. Therefore, the HCG@Cu/Zn-MOF hydrogel has shown significant potential as a wound dressing for effective diabetic wound healing.

Methods

Materials

$Zn(NO_3)_2{\cdot}6H_2O$ (98%), $Cu(NO_3)_2{\cdot}3H_2O$ (98%), 2-methylimidazole (99%), HPMC (6 mPa·s), CS (degree of deacetylation ≥95%, viscosity 100–200 mPa·s), JC-10 mitochondrial membrane potential probe, GLY, methanol, H_2O_2, and ethanol were purchased from Aladdin Chemical Reagents (China). Xanthine oxidase (from milk, ≥0.4 units/mg protein) and reduced glutathione (GSH; ≥98.0%) were purchased from Sigma-Aldrich. Hoechst 33342 live-cell staining solution was purchased from Beyotime Biotechnology (Shanghai, China). Nitrotetrazolium blue chloride (NBT, 98%), ascorbic acid (AsA), xanthine (98%), cysteine (≥98%), and 2′,7′-dichlorodihydrofluorescein diacetate (DCFH-DA) were purchased from Aladdin Co. Ltd 5,5′-Dithiobis(2-nitrobenzoic acid) (DTNB) was purchased from JK Scientific. The Cell Counting Kit 8 (CCK-8) was purchased from Solarbio (Beijing, China). All water used in experiments was purified using a Milli-Q purification system (Millipore, USA). All reagents were used without further purification unless otherwise specified.

Preparation of copper–zinc metal–organic framework

A total of 0.660 g (8 mmol) of 2-methylimidazole was dissolved in 11 ml of methanol. Separately, 0.223 g of $Zn(NO_3)_2{\cdot}6H_2O$ and 0.060 g of $Cu(NO_3)_2{\cdot}3H_2O$ (totaling 1 mmol) were dissolved in another 11 ml of methanol. The two solutions were mixed and stirred at room temperature for 3 h. After centrifugation at 8000 rpm for 10 min, the precipitate was collected, washed three times with methanol, and dried under vacuum at 60°C. The final product was designated Cu/Zn-MOF. For comparison, $Zn(NO_3)_2{\cdot}6H_2O$ without the addition of $Cu(NO_3)_2{\cdot}3H_2O$ was used to synthesize ZIF-8.

Characterization of copper–zinc metal–organic framework nanoparticles

The morphology, lattice fringes, and elemental distribution of Cu/Zn-MOF and ZIF-8 were examined by field-emission scanning electron microscopy (FE-SEM; HITACHI S-4800, Japan) and transmission electron microscopy (TEM; FEI Talos F200X, USA). Energy-dispersive X-ray spectroscopy (EDS) was performed for elemental mapping of Cu and Zn. The phase composition and crystal structure were analyzed by wide-angle X-ray diffraction (XRD), whereas the chemical composition was determined by X-ray photoelectron spectroscopy (XPS). A nanoparticle-size analyzer was used to measure the particle size and distribution.

Preparation of HCG@Cu/Zn-MOF gel

HPMC, CS, and GLY were incorporated after Cu/Zn-MOF was uniformly dispersed in phosphate-buffered saline (PBS) buffer. The mixture was then stirred at 65°C until fully dissolved and cooled to 4°C overnight to form hydrogels. The CS and GLY contents were fixed at 1 and 30 wt%, respectively, whereas HPMC and Cu/Zn-MOF were varied between 4–8 wt% and 0–3 wt%, respectively.

Gel-forming behavior test of the HCG@Cu/Zn-MOF gels

The gel-forming process involved adding the hydrogel's precursor solution to a glass container at ambient temperature (25°C), heating the containers to 37°C in a water bath, and then inverting the container to determine if gelation of the hydrogel occurred. The hydrogels were then immediately lyophilized and frozen in liquid nitrogen, and the samples were coated with gold sputtering to enhance conductivity. Next, the internal configuration of the HCG@Cu/Zn-MOF hydrogels was examined by SEM (HITACHI S-4800, Japan). Testing and analysis were performed on the hydrogels' infrared spectra. The rheological properties of the HCG@Cu/Zn-MOF gels were investigated, and the heat-sensitive transition behavior of the gels was evaluated. The energy storage modulus (G′) and loss modulus (G″) of the HCG@Cu/Zn-MOF gels were determined by rheometry, and the gelation temperature of the resulting gels was determined. Temperature scans were conducted by heating the hydrogel from 20°C to 80°C at a rate of 1°C/min. The junction of the G′ and G″ curves determined the gelation temperature. In addition, the same technique was used to test the viscosity of the HCG@Cu/Zn-MOF gels from 25°C to 60°C, and frequency scans were performed from 0.1 to 10 Hz.

Ion-release behavior of copper–zinc metal–organic framework in different environments

To simulate different *in vivo* and *in vitro* environments, PBS, Dulbecco's modified Eagle medium (DMEM) supplemented with fetal bovine serum (FBS), and HCG extracts were used. Cu/Zn-MOF was added at a final concentration of 1 mg/ml, and inductively coupled plasma (ICP) optical emission spectroscopy was used to measure the release of Cu^{2+} and Zn^{2+} ions over days 1–5.

Swelling behavior of HCG@Cu/Zn-MOF gel

The HCG@Cu/Zn-MOF hydrogels' swelling behavior was evaluated by immersing samples in PBS at 37°C until swelling equilibrium was reached. Samples were removed and weighed after 12, 24, and 48 h of immersion. After surface water was removed, the swelling ratio was calculated according to the following formula:

$$\text{Swelling ratio } (\%) = \frac{W_t - W_0}{W_0} \times 100\%,$$

where W_t is the hydrogel weight at a given time and W_0 is the initial weight.

Downloaded from academic.oup.com/burnstrauma/article/doi/10.1093/burnst/tkaf076/8341464 by guest on 12 October 2026

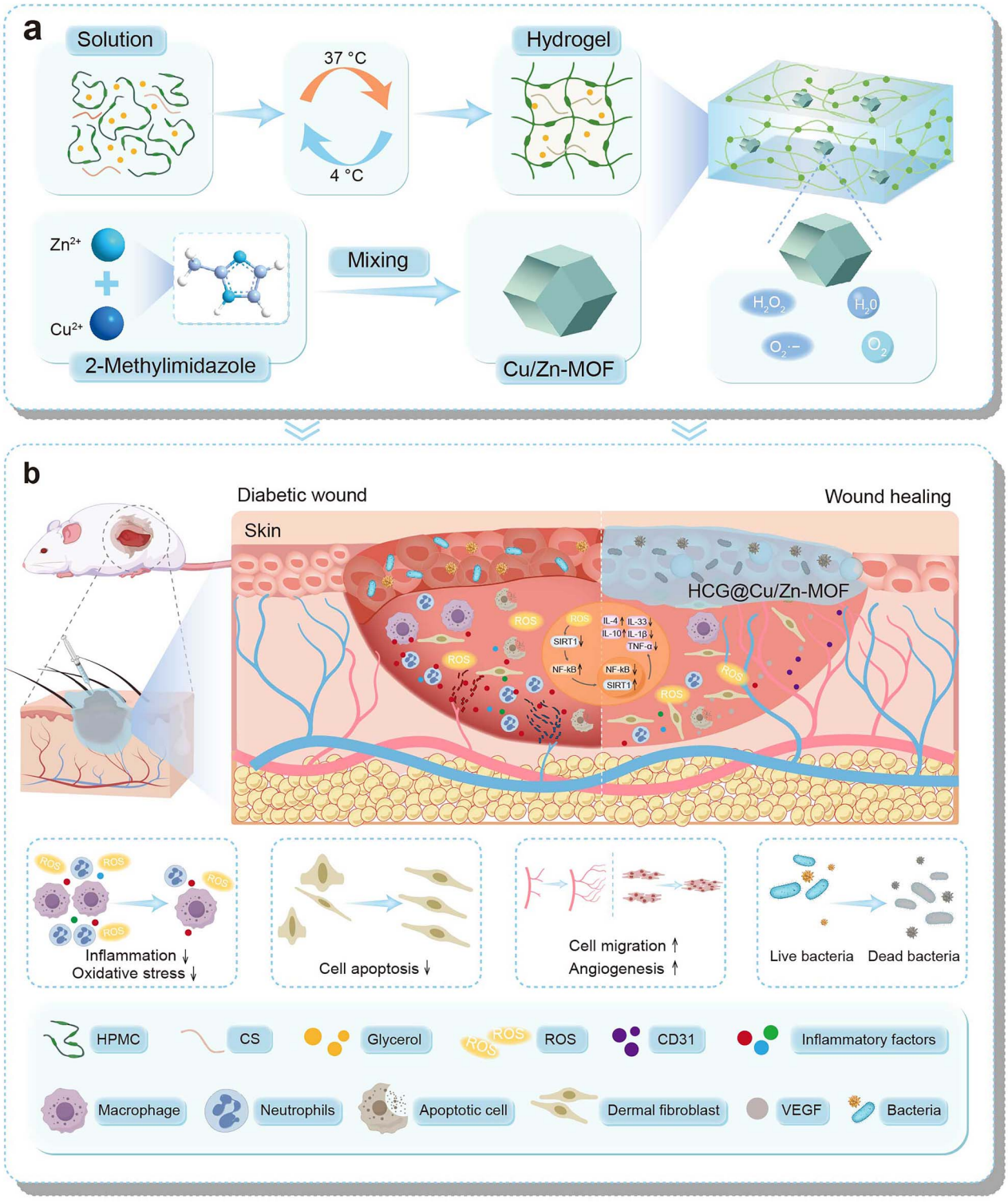


Figure 1. Schematic illustration of a temperature-sensitive hydrogel loaded with Cu/Zn-MOF nanoparticles for diabetic wound therapy. (a) Preparation of the HCG@Cu/Zn-MOF hydrogel and schematic representation of its antioxidant mechanism. (b) Multifunctional properties of the HCG@Cu/Zn-MOF hydrogel in promoting wound healing, including ROS clearance, anti-inflammatory and anti-apoptotic effects, antibacterial activity, and stimulation of angiogenesis and fibroblast migration. *HCG* hydroxypropyl methylcellulose chitosan glycerol

Hydrophilicity test of the HCG@Cu/Zn-MOF gel

An OCA15EC device was used to measure the contact angle of the samples. Each sample was placed flat on the measuring platform at 37°C, and a microsyringe was used to apply 3-μl droplets of distilled water. After ~10 s, the droplet was photographed and analyzed.

Downloaded from academic.oup.com/burnstrauma/article/doi/10.1093/burnst/tkaf076/8341464 by guest on 12 October 2026

Enzyme-like activity of the HCG@Cu/Zn-MOF gel

SOD-like activity: NBT is reduced to a blue precipitate by O_2^-; therefore, the amount of O_2^- was measured by NBT to characterize SOD-like activity. A 500-μl aliquot of HCG@Cu/Zn-MOF hydrogel extract was mixed with 25 mM xanthine, 2.375 U/ml xanthine oxidase, and 100 μg/ml NBT in Tris–HCl buffer (pH 7.6). The absorbance at 550 nm was continuously recorded for 5 min.

$$\text{Inhibition } (\%) = (A_0 - A)/A_0 \times 100\%,$$

where A is the absorbance in the presence of the hydrogel and A_0 is the absorbance without hydrogel.

The catalytic performance of the HCG@ZIF-8 hydrogel was also evaluated. The Tris–HCl buffer pH was varied to investigate its influence on SOD-like activity. Electron paramagnetic resonance (EPR) spectroscopy was performed from 3 to 15 min, with 5,5-dimethyl-1-pyrroline N-oxide as the O_2^- trapping agent.

Glutathione peroxidase (GPx)-like activity: GSH depletion was assessed using microspectrophotometry with DTNB as a probe. H_2O_2 solution (0.8 mM, 500 μl) was added to 1.0-mM GSH in PBS, followed by 500 μl of HCG@Cu/Zn-MOF hydrogel extract. After incubation of 10 min, 100 μl of 2.5 mM DTNB was added to 200 μl of the mixture, and the absorbance at 412 nm was recorded. The catalytic properties of the HCG@ZIF-8 hydrogel were evaluated using the same procedure. The pH of PBS was adjusted to investigate its effect on GPx-like activity. Furthermore, GSH concentrations were varied (0.3125–80 mM), absorbance at 412 nm was measured, and the data were analyzed using Michaelis–Menten fitting and plotted on a Lineweaver–Burk curve.

Thiol peroxidase e (TPx)-like activity: Cysteine (0.2 mM), H_2O_2 (0.8 mM), and 500 μl of the HCG@Cu/Zn-MOF hydrogel extract were mixed in PBS (pH 7.4). After incubation, 200 μl of the mixture was added to 100 μl of 2.5-mM DTNB. The absorbance at 412 nm was used to determine cysteine depletion. The catalytic properties of the HCG@ZIF-8 hydrogel were also evaluated. The pH of PBS was adjusted to evaluate its effect on TPx-like activity.

Ascorbate peroxidase (APx)-like activity: The breakdown of AsA at 290 nm in the presence of H_2O_2 and a catalyst was measured to determine APx-like activity. The reaction mixture contained AsA (0.2 mM), H_2O_2 (10 mM), and 500 μl of either HCG@Cu/Zn-MOF or HCG@ZIF-8 hydrogel in PBS. The effect of pH on APx-like activity was investigated by adjusting the pH of PBS. The H_2O_2 concentration was varied from 0.3125 to 80 mM, the absorbance at 290 nm was measured, and the data were subjected to Michaelis–Menten fitting and plotted on a Lineweaver–Burk curve. The EPR assay was performed from minutes 3–15 utilizing TEMP as the H_2O_2 trapping agent.

Density functional theory calculation

Spin-polarized geometry optimization calculations based on first principles were performed according to density functional theory (DFT) by use of the Vienna Ab Initio Simulation Package. The frozen-core projector augmented-wave method was used to describe interactions between atomic cores and valence-electron density. The exchange-correlation potential was approximated by use of the generalized gradient approximation with the Perdew–Burke–Ernzerhof function to calculate electron–electron interactions. A kinetic energy cutoff of 450 eV was applied to ensure convergence. Strong correlation effects of transition metals were corrected by use of the DFT + U method, with U values of 4 and 7.5 applied to the 3d orbitals of Cu and Zn, respectively. A $1 \times 1 \times 1$ k-point grid was used to sample the Brillouin zone. The conjugate gradient method was employed for structural relaxation, simultaneously minimizing total energy and interatomic forces. The convergence tolerance for total energy was set to 10^{-5} eV, and the residual force on each atom was constrained to <0.05 eV/Å. Dispersion-corrected DFT-D3 schemes were further used to account for van der Waals interactions.

The absorption energy (E_{abs}) can be calculated as follows:

$$E_{ads} = E\text{catalysts} + \text{adsorbates} - E\text{catalysts} - E\text{adsorbates},$$

where *E*catalysts is the energy of Cu/Zn-MOF, *E*adsorbates is the energy of molecules adsorbed, and *E*catalysts + adsorbates is the energy of the absorbed structures.

Reactive oxygen species–scavenging capacity of HCG@Cu/Zn-MOF gel

To mimic a pathological ROS environment, L929 cells were treated with lipopolysaccharide (LPS) [41]. The DCFH-DA fluorescent probe penetrates the cell membrane, reacts with intracellular ROS, and emits green fluorescence. Cells were seeded into 12-well plates, after which 0.2 ml of hydrogel was added to each well and incubated with 1 ml of DMEM containing LPS (1 μg/ml). After 24 h, the cells were incubated with DCFH-DA for 30 min and Hoechst dye for 10 min, followed by washing with PBS. Intracellular ROS levels were then observed under an inverted fluorescence microscope, and fluorescence intensity was quantified by flow cytometry.

In vitro biocompatibility

Biocompatibility was evaluated by performing the CCK-8 assay to assess cell viability. L929 and human umbilical vein endothelial cells (HUVECs) were seeded into 96-well plates and incubated for 24 h. The culture medium was replaced with hydrogel extract, and the cells were further incubated for 24 or 48 h. After removing the medium, each well was supplemented with 100 μl of fresh DMEM containing 10 μl of CCK-8 reagent and incubated for 4 h. A microplate reader was used to measure UV absorbance at 450 nm.

$$\text{Cell viability } (\%) = (A_s - A_b)/(A_c - A_b) \times 100\%,$$

where A_s, A_c, and A_b represent the optical density (OD) values of the cells cultured in hydrogel extract, DMEM, and cell-free DMEM, respectively.

Live/dead staining

After an initial 24-h incubation, the L929 cells were cultured for an additional 12, 24, or 48 h in medium containing hydrogel extract. The cells were stained with a live/dead kit following the manufacturer's instructions and examined under a microscope.

Hemolysis test *in vitro*

Anticoagulated blood was prepared by mixing 20 ml of blood with 1 ml of 2% (w/v) potassium oxalate saline. Test blood was prepared by mixing 5 ml of saline with 4 ml of

Downloaded from academic.oup.com/burnstrauma/article/doi/10.1093/burnst/tkaf076/8341464 by guest on 12 October 2026

anticoagulated blood. Subsequently, 0.1 ml of diluted blood was added to 5 ml of hydrogel extract and incubated for 2 h. After centrifugation, the absorbance at 540 nm was measured to calculate the hemolysis rate.

$$\text{Hemolysis rate } (\%) = (A_s - A_n) / (A_p - A_n) \times 100,$$

where A_s, A_n, and A_p are the absorbance values of PBS, Triton X, and hydrogel extract, respectively.

Cell migration

A scratch assay was used to evaluate the effect of the hydrogel on L929-cell migration. L929 cells were cultured to full confluence after seeding into six-well plates. The monolayers were scratched with a 200-μl pipette tip and washed twice with PBS. Subsequently, 2 ml of hydrogel extract was added to the cells. Cell migration was observed under a microscope at 0, 12, and 24 h, and ImageJ software was used to quantify migratory behavior. Additionally, L929 cells were cultured in high-glucose medium and passaged for three generations before undergoing migration assays.

$$\text{Migration percentage } (\%) = (1 - S_t/S_0) \times 100\%,$$

where S_0 is the initial wound area and S_t is the unhealed area.

Cell-apoptosis assay

The cells were treated as described in Section 2.11, stained with JC-10, and examined under a fluorescence microscope to detect red or green fluorescence. An Annexin V-FITC Apoptosis Detection Kit was used to evaluate the protective effect of hydrogel samples against HUVEC apoptosis. Flow cytometry was used to quantify the apoptosis rate. HUVEC cells were cultured in high-glucose medium for three generations to mimic the diabetic microenvironment and were subsequently subjected to JC-10 staining and apoptosis assays via flow cytometry.

In vitro angiogenesis

To evaluate the vasculogenic potential of hydrogels, HUVECs (1×10^5 cells/well) were cultured in six-well plates for 24 h. The medium was replaced with 1 ml of extracts from HCG, HCG@ZIF-8, or HCG@Cu/Zn-MOF hydrogels, and the cells were incubated for an additional 24 h. Subsequently, the cells were trypsinized and reseeded into 96-well plates (3×10^4 cells/well) pre-coated with matrix gel and incubated for 4 h. After incubation, the cells were observed under a microscope. ImageJ software was used to quantify the numbers of nodes and branches.

Evaluation of *in vitro* antimicrobial resistance

The antimicrobial properties of the hydrogels were evaluated against *E. coli* and *S. aureus* as model organisms. Bacterial suspensions (10^9 CFU/ml) were inoculated into 96-well plates and co-cultured with hydrogel precursor solutions for 12 h. After incubation, the suspensions were collected, diluted to 10^5–10^2 CFU/ml, and 5 μl of each dilution was spread onto tryptic soy-broth agar plates, followed by incubation at 37°C for 12 h. Bacterial survival was determined by calculating the survival rate. Hydrogel-treated bacterial samples were stained with PI (dead cells) and SYTO™-9 (live cells), incubated in the dark for 30 min, and observed under a fluorescence microscope. For morphological analysis, *E. coli* and *S. aureus* were co-cultured with hydrogels, fixed with 2.5% glutaraldehyde, and dehydrated through graded ethanol. SEM was performed to examine the bacterial surface structure and integrity. PBS-treated bacteria served as controls, and all experiments were performed in triplicate.

Full-thickness diabetic wound-repair assay

All mouse experiments were conducted in accordance with the National Regulations for the Control of Laboratory Animals. Diabetes was induced in adult male ICR mice (18–24 g) by intraperitoneal injection of streptozotocin (STZ, 60 mg/kg) for five consecutive days. A glucometer was used to monitor blood glucose levels every other day, starting 3 days after the final STZ injection. Mice with blood glucose levels above 16.7 mM in at least two consecutive measurements were classified as diabetic.

Before operation, a gas anesthetic machine was used to put all animals to sleep with isoflurane. The dorsal skin of each mouse was shaved and disinfected with 75% ethanol. A full-thickness circular wound (10-mm diameter) was created. To simulate infection, 10 μl of *S. aureus* suspension (10^9 CFU/ml) was applied dropwise to the wound. Saline, HCG, HCG@ZIF-8, Cu/Zn-MOF, or HCG@Cu/Zn-MOF gels were applied to the wound surface. Wound closure was recorded on days 0, 3, 7, 10, and 14.

$$\text{Wound closure rate } (\%) = (S_0{}^{-}S_t) / S_0 \times 100\%,$$

where S_0 is the initial wound area (day 0) and S_t is the wound area on a given day.

The wound tissues collected on days 7 and 14 were sectioned at 5 μm and subjected to hematoxylin and eosin (H&E) and Masson staining for histology, dihydroethidium (DHE) staining for ROS detection, and immunofluorescence staining [CD31 and vascular endothelial growth factor (VEGF)] to analyze angiogenesis *in vivo*. Staining with H&E was also performed on heart, liver, spleen, lung, and kidney tissues. Blood was collected for hematology and biochemistry to assess the *in vivo* biocompatibility of the hydrogels.

Western blot

Cells were lysed, and a BCA Protein Assay Kit (Aladdin Chemical Reagents, China) was used to analyze wound tissues from day 3 for protein concentration. Equal amounts of protein (4 μg/μl, 20 μl) were heated at 100°C for 10 min and loaded onto a 10% sodium dodecyl sulfate–polyacrylamide gel electrophoresis gel. Proteins were transferred from the gel to a polyvinylidene fluoride membrane, incubated overnight at 4°C with anti-rabbit Sirt1 (Abcam, ab110304) and nuclear factor-κ beta (NF-κB) (Abcam, ab288751) antibodies, and followed by incubation with the corresponding secondary antibodies for 2 h and subsequent development. ImageJ software was used to analyze the band intensities, and the data were normalized.

Statistical analysis

All experiments were performed with at least three independent replicates. Quantitative data are expressed as mean ± standard deviation. Enzyme kinetic parameters (K_m and V_{max}) were obtained by fitting experimental data to the

Downloaded from academic.oup.com/burnstrauma/article/doi/10.1093/burnst/tkaf076/8341464 by guest on 12 October 2026

Michaelis–Menten model. The fitting process used nonlinear regression analysis in Origin 2023 software. Lineweaver–Burk plots were generated via double-reciprocal linear fitting. Statistical analyses using one-way and two-way analysis of variance (ANOVA) were performed in GraphPad Prism (version 10.1.2) and Origin 2023 software. Tukey's test was performed for post hoc pairwise comparisons. A *P*-value <0.05 was considered statistically significant, and 'ns' indicated no significant difference. The symbols *, **, ***, and **** denote $P < 0.05$, 0.01, 0.001, and 0.0001, respectively.

Results

Characterization of copper–zinc metal–organic framework nanoparticles

To synthesize copper-mimetic nanoenzymes (Cu/Zn-MOF), copper ions were incorporated into MOFs formed by the self-assembly of zinc ions and dimethylimidazole at room temperature (Figure 2a). The SEM images revealed that the synthesized ZIF-8 nanoparticles had a rhombic dodecahedral structure (Figure 2b). The Cu/Zn-MOF nanoparticles prepared by copper incorporation retained the morphological features of ZIF-8 (Figure 2c), with an average diameter of ∼336.47 nm and a polydispersity index <0.3, indicating good dispersibility (Figure 2d). Confirmation that the scattering pattern corresponded to the single-crystal nature of Cu/Zn-MOF, with a lattice spacing of 0.537 nm, was achieved by performing TEM combined with selected area electron diffraction (Figure 2e and f). High-angle annular dark-field scanning TEM and elemental mapping (Figure 2g) showed homogeneous element distribution in Cu/Zn-MOF. TEM-EDS showed 31.62% Zn and 2.61% Cu (Figure S1, see online supplementary material), confirming successful copper-ion incorporation. Additionally, characteristic peaks of Cu 2p and Zn 2p were observed in the XPS spectra. The high-resolution Cu 2p spectra (Figure 2h) showed two main peaks with two satellite peaks, with binding energies of Cu $2p_{1/2}$ and Cu $2p_{3/2}$ at approximately 951.98 and 932.68 eV, respectively. These results indicated the coexistence of Cu^{+} and Cu^{2+}, suggesting potential antioxidant activity. The Zn 2p spectra (Figure 2i) showed two main peaks corresponding to Zn $2p_{1/2}$ and Zn $2p_{3/2}$, with binding energies of approximately 1044.58 and 1021.68 eV, confirming the successful construction of Cu/Zn-MOF. The crystal structure and phase purity of ZIF-8 and Cu/Zn-MOF were characterized from the XRD patterns (Figure 2j). The standard ZIF-8 diffraction pattern is characterized by crystalline planes (011), (002), (222), and (134). The XRD patterns of Cu/Zn-MOF and ZIF-8 were consistent with the standard reference, confirming excellent phase purity and indicating that minor Cu doping did not significantly affect the ZIF-8 structure. The zeta potential analysis of the Cu/Zn-MOF nanoparticles at different pH levels (Figure S2, see online supplementary material) revealed that the surface charge increased progressively with increasing pH values above 3, and maximum stability was observed under mildly acidic conditions.

Thermosensitive HCG@Cu/Zn-MOF gel transition behavior

A temperature-responsive hydrogel based on HPMC was developed for the treatment of irregular diabetic wounds. The HPMC solution exhibited temperature-dependent reversible sol–gel transition behavior. Below the lower critical solution temperature (LCST), a homogeneous solution was formed, but above the LCST, the solution transformed into a network-like gel structure [42]. However, the HPMC solutions' LCST of approximately 60°C is significantly greater than human body temperature and does not meet the requirements for using the best biological phase-change materials. Therefore, we used PBS buffer to dissolve HPMC to induce the 'salting-out' effect and added a certain proportion of GLY to reduce the LCST value. For ease of description in this paper, we refer to the hydrogels as follows: HPMC only as HPMC gel; HPMC and CS as HC gel; HPMC, CS, and GLY as HCG gel; and MC, CS, GLY, and Cu/Zn-MOF as HCG@Cu/Zn-MOF gel. Each element's concentration is indicated by the numbers in the acronym.

Initially, the LCST values of the HPMC, HC, HCG, and HCG@Cu/Zn-MOF gels were determined by rheometry. The LCST of the HPMC gels decreased from 58.1°C to 55.1°C with increasing HPMC content (4–8 wt%) (Figure 3a). After the addition of 1 wt% CS to the HPMC gel, LCST values of 45.1°C–47.2°C were observed (Figure 3b), remaining considerably higher than physiological temperature. To further reduce the LCST, 30 wt% GLY was added to the HC gels, resulting in a marked decrease, with values ranging from 34.1°C to 38.2°C (Figure 3c). The LCST of the 8HCG gel was 38.2°C, remaining above physiological temperature; therefore, the 6HCG hydrogel, with an LCST below physiological temperature, was selected for subsequent Cu/Zn-MOF loading.

After loading different amounts of Cu/Zn-MOF nanoparticles, the LCST values of the 6HCG@1Cu/Zn-MOF, 6HCG@2Cu/Zn-MOF, and 6HCG@3Cu/Zn-MOF gels decreased to 34.6°C, 36.1°C, and 35.9°C, respectively, all below the body temperature (Figure 3d). At 37°C, all three hydrogels exhibited comparatively low viscosity, indicating favorable injectability under physiological conditions (Figure 3e). The energy storage modulus of these hydrogels varied between 30 and 800 Pa, and all three nanoparticle-loaded gels responded to frequency changes by undergoing gel-to-sol transitions with increasing frequency (Figure S3, see online supplementary material), demonstrating excellent injectability and typical shear-thinning properties. Photographs of the sol–gel transition in the 6HCG and 6HCG@2Cu/Zn-MOF gels showed good flowability at 4°C, solidification at 37°C, and uniform dispersion of the Cu/Zn-MOF nanoparticles within the hydrogels (Figure 3f). The effects of CS and GLY on the structure of the HPMC gels also were investigated. FTIR analysis revealed characteristic peaks of HPMC, CS, and GLY in the HCG gel, indicating that simple mixing did not alter the structural framework of the original HPMC hydrogel (Figure 3g). Simulations of *in vivo* and *in vitro* environments were conducted, and ICP analysis was performed to quantify Cu and Zn release. In PBS, the release rate peaked at day 3, whereas ion release was slower in the DMEM + FBS and HCG environments, reaching maximum levels at day 5 (Figure S4, see online supplementary material). The dispersion of Cu/Zn-MOF in different environments was also recorded photographically. As shown in Figure S5, Cu/Zn-MOF began to precipitate in PBS at 2 h, with the supernatant gradually becoming transparent. In DMEM + FBS, simulating the *in vivo* environment, precipitation occurred at 24 h. In the HCG environment, Cu/Zn-MOF remained well dispersed at 48 h,

Downloaded from academic.oup.com/burnstrauma/article/doi/10.1093/burnst/tkaf076/8341464 by guest on 12 October 2026

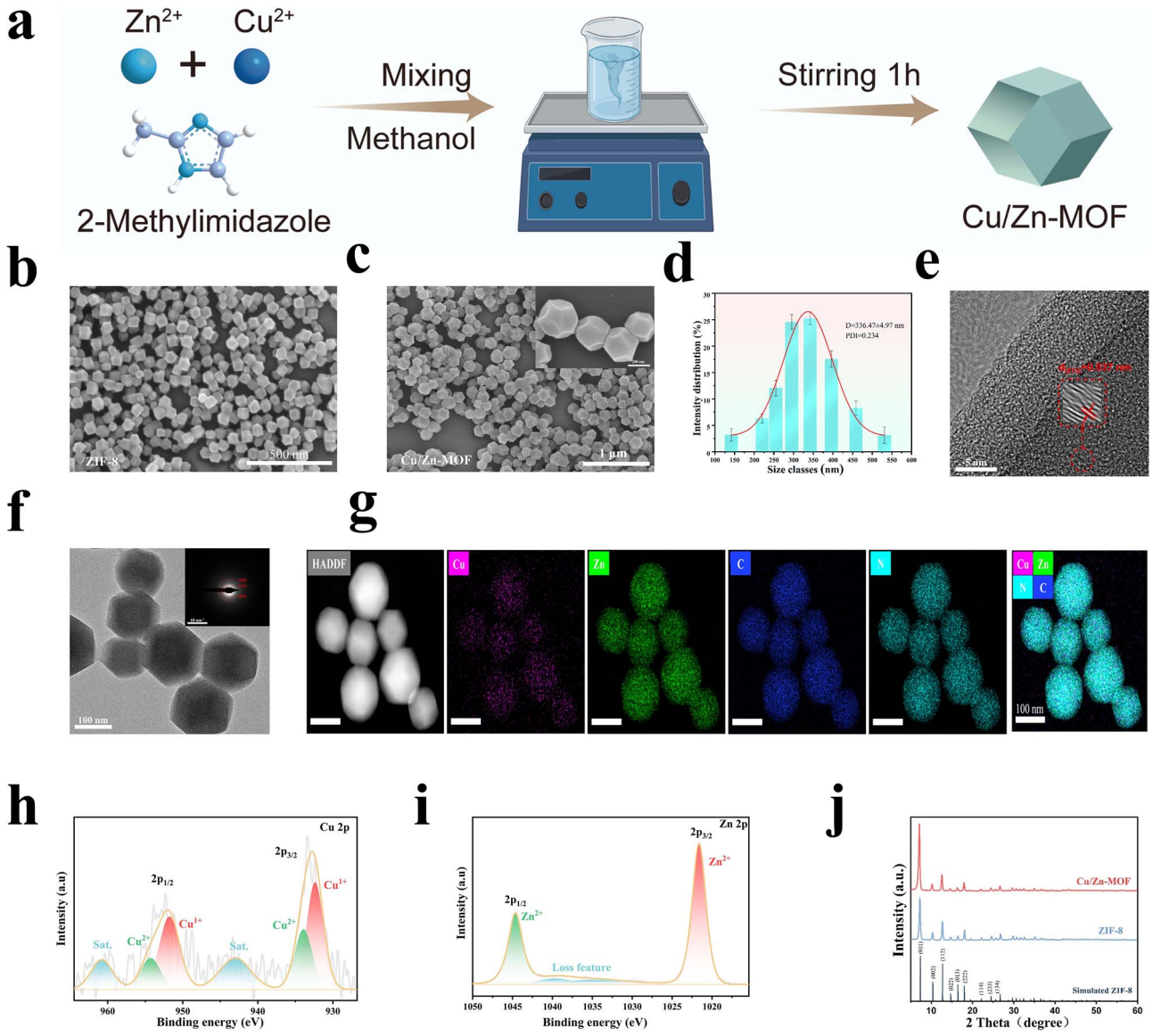


Figure 2. Characterization of ZIF-8 and Cu/Zn-MOF. (a) Schematic illustration of Cu/Zn-MOF synthesis. (b) SEM micrograph of ZIF-8 (Scale bar: 500 nm). (c) SEM micrograph of Cu/Zn-MOF (Scale bar: 5 nm). (d) Particle-size distribution of Cu/Zn-MOF. (e) TEM micrograph of Cu/Zn-MOF (Scale bar: 5 nm). (f) Selected area electron diffraction pattern of Cu/Zn-MOF with corresponding crystallographic analysis (Scale bar: 100 nm). (g) HAADF-STEM micrograph and corresponding EDX elemental mapping of the Cu/Zn-MOF nanocatalyst (Scale bar: 1 μm). (h and i) XPS narrow scans of Cu/Zn-MOF. (j) XRD patterns of Cu/Zn-MOF and ZIF-8. All data are presented as mean ± SD. *ns* not significant; $^{*}P < 0.05$; $^{**}P < 0.01$; $^{***}P < 0.001$; $^{****}P < 0.0001$. *SD* standard deviation, *ZIF* zeolitic imidazolate framework, *MOF* metal–organic framework, *SEM* scanning electron microscopy, *TEM* transmission electron microscopy, *XPS* X-ray photoelectron spectroscopy

maintaining a turbid suspension. These findings indicate that Cu/Zn-MOF exhibited enhanced stability after incorporation into the HCG hydrogel, thereby enabling sustained release. The incorporation of nanoparticles within the hydrogel improved stability, allowing controlled release and prolonged pro-healing effects on wounds.

Additionally, the swelling behavior, injectability, and surface properties of the hydrogels were examined. Photographic evidence and swelling ratio data indicated that 6HCG, 6HCG@1Cu/Zn-MOF, 6HCG@2Cu/Zn-MOF, and 6HCG@3Cu/Zn-MOF reached swelling equilibrium at 48 h, with a swelling ratio of 27% (Figure 3h). Photographs further demonstrated that 6HCG@2Cu/Zn-MOF formed a gel in water at 37°C and could be injected through a 25G needle, allowing remodeling into various shapes and facilitating the filling and coverage of deep irregular wounds (Figure 3i). The contact angle, an important indicator of surface hydrophilicity, was measured for all four hydrogels. Photographs showed that the contact angles were $< 90°$ (Figure 3j), confirming good hydrophilicity. Increasing Cu/Zn-MOF loading did not significantly alter the contact angle of the 6HCG@1Cu/Zn-MOF, 6HCG@2Cu/Zn-MOF, or 6HCG@3Cu/Zn-MOF gels, indicating consistently high hydrophilicity, which is beneficial for maintaining a moist wound environment and promoting cell migration.

Multi-species enzymatic activity of HCG@Cu/Zn-MOF hydrogels

Superoxide anion (O_2^-) is the initiating molecule of ROS bursts, whereas SOD primarily catalyzes the disproportionation of O_2^- into H_2O_2 and O_2, serving as the first step in

Downloaded from academic.oup.com/burnstrauma/article/doi/10.1093/burnst/tkaf076/8341464 by guest on 12 October 2026

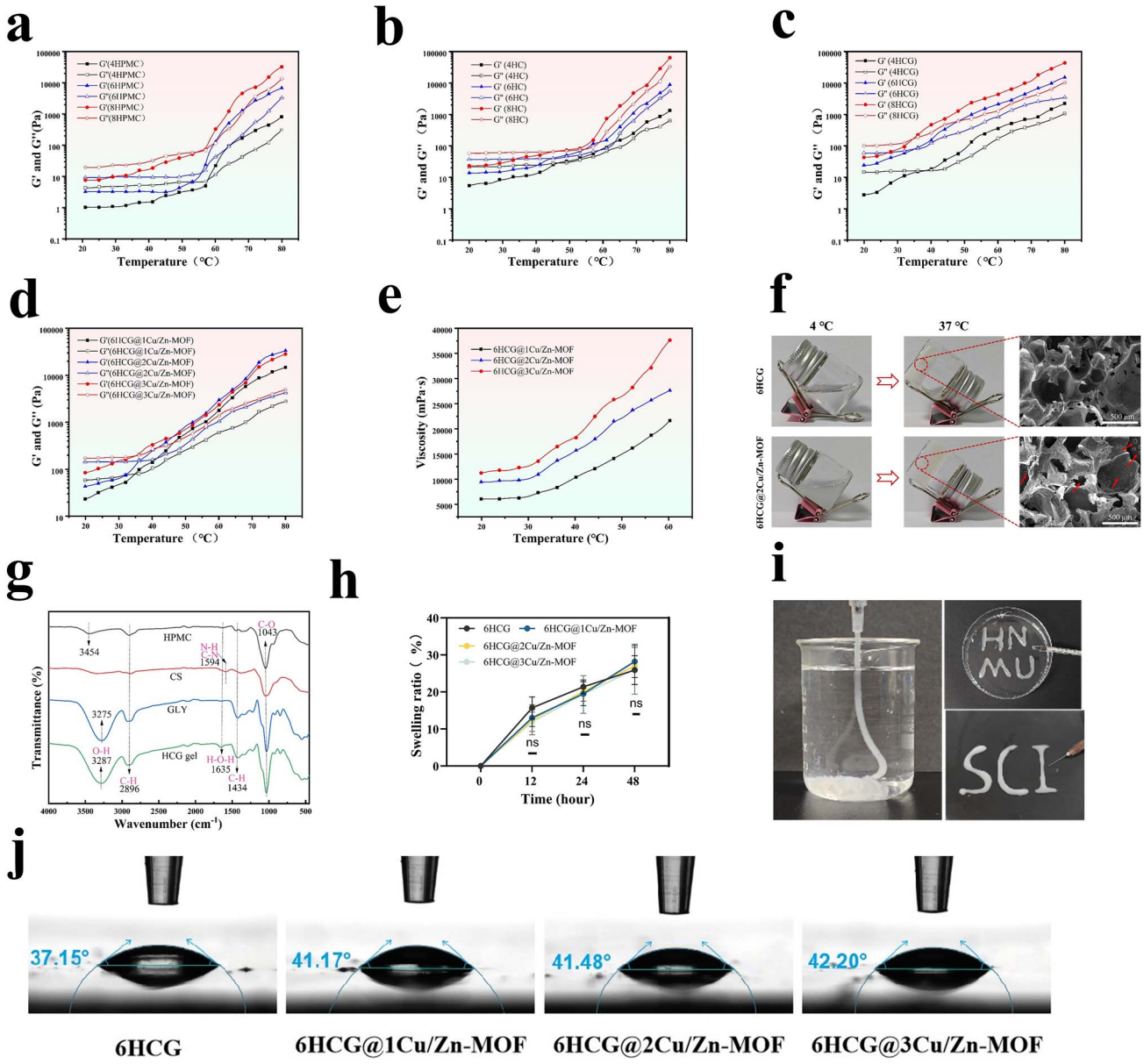


Figure 3. Characterization of HCG@Cu/Zn-MOF hydrogels. (a–d) Rheological analysis of the thermosensitive sol–gel transition behavior of HPMC, HC, HCG, and HCG@Cu/Zn-MOF hydrogels. Gelation temperature was determined at the intersection of the storage modulus (G′) and loss modulus (G″) curves. (e) Viscosity of the hydrogel after incorporation of Cu/Zn-MOF nanoparticles. (f) Thermosensitive transition behavior and SEM micrographs of the hydrogels. Red arrows indicate Cu/Zn-MOF nanoparticles. Scale bar: 500 μm. (g) FTIR spectra of HPMC, CS, GLY, and HCG hydrogels. (h) Swelling behavior of the hydrogels. (i) Gel-forming behavior of HCG@Cu/Zn-MOF hydrogel in water at 37°C, demonstrating injectability and shape adaptability. (j) Contact angle measurements of the hydrogels. All data are presented as mean ± SD. *ns* not significant; $^{*}P < 0.05$; $^{**}P < 0.01$; $^{***}P < 0.001$; $^{****}P < 0.0001$. Statistically significant differences in the experimental data were determined by performing two-way ANOVA and Tukey's post hoc test. *SD* standard deviation, *ZIF* zeolitic imidazolate framework, *MOF* metal–organic framework, *SEM* scanning electron microscopy, *HCG* hydroxypropyl methylcellulose chitosan glycerol, *HPMC* hydroxypropyl methylcellulose, *CS* chitosan, *GLY* glycerol

antioxidant defense (Figure 4a) [43, 44]. NBT reacts with O_2^- to produce a dark blue-colored aliquot of formazan with an absorption wavelength of 550 nm [45]. Therefore, colorimetric assays were performed to evaluate SOD-like activity. All three HCG@Cu/Zn-MOF hydrogels exhibited O_2^- scavenging capability and demonstrated SOD-like activity superior to that of HCG@ZIF-8 (6 wt% HPMC, 1 wt% CS, 30 wt% GLY, 2 wt% ZIF-8) (Figure 4b). Notably, increasing the Cu/Zn-MOF content from 2 to 3 wt% enhanced O_2^- scavenging only from 88.2% to 90.7%, indicating no significant improvement in SOD-like activity. The effect of pH on SOD-like activity was also examined, and Figure S6a shows that the alkaline environment adversely affected the SOD-like characteristics of HCG@Cu/Zn-MOF as pH increased, thereby reducing O_2^- elimination efficiency.

As a byproduct generated by HCG@Cu/Zn-MOF during scavenging O_2^-, H_2O_2 can still induce oxidative stress and inflammation in cells; therefore, its subsequent removal is also critical. As an important peroxidative disintegrative enzyme in the organism, GPx reduces H_2O_2 to H_2O with the involvement of GSH [46] (Figure 4a). To evaluate GPx-like activity, DTNB was used, which reacts with the sulfhydryl groups

Downloaded from academic.oup.com/burnstrauma/article/doi/10.1093/burnst/tkaf076/8341464 by guest on 12 October 2026

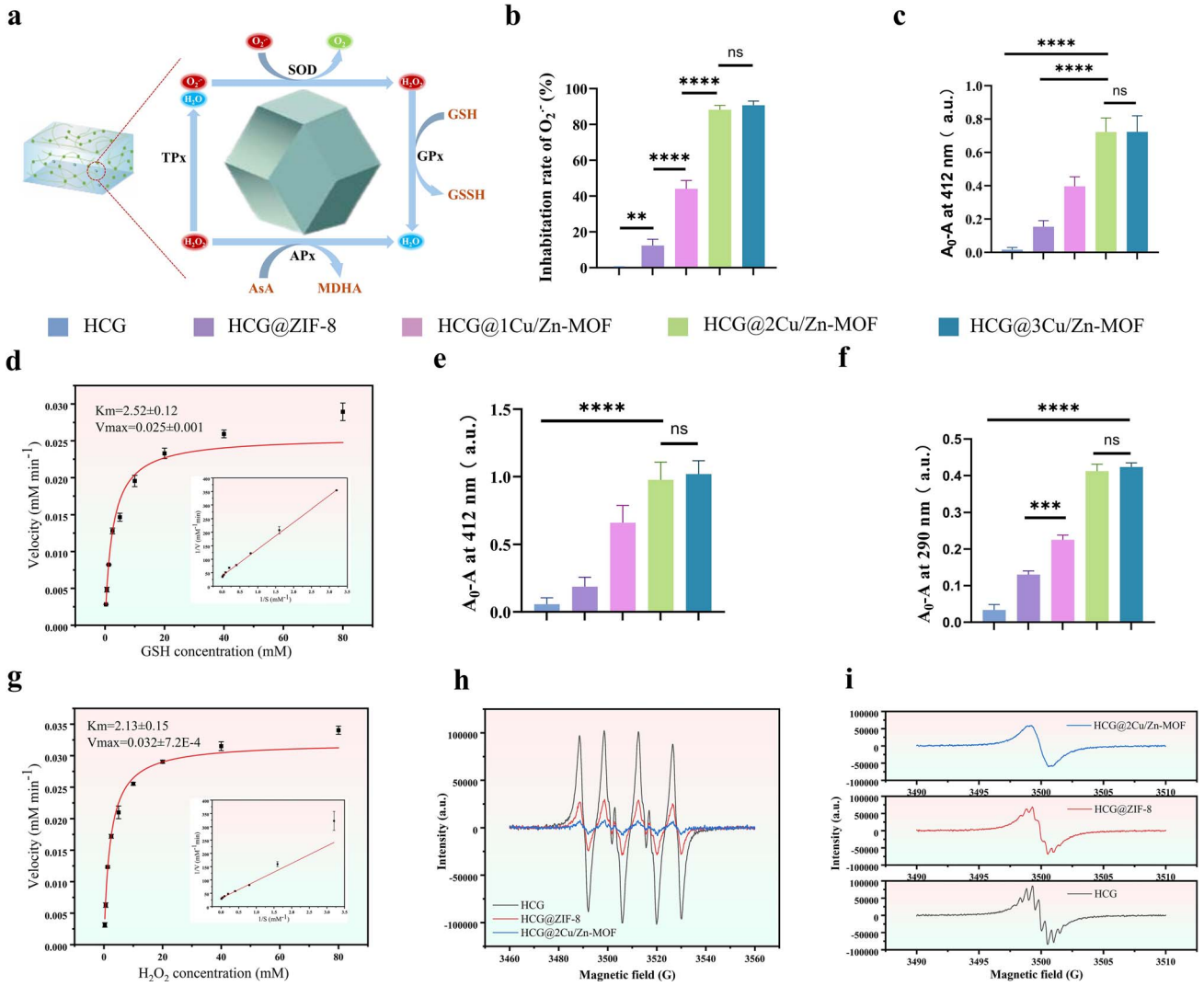


Figure 4. Multi-enzyme activity of HCG@Cu/Zn-MOF hydrogels. (a) Schematic illustration of reactive oxygen cascade scavenging by HCG@Cu/Zn-MOF. (b) SOD-like activity of HCG@Cu/Zn-MOF and HCG@ZIF-8 ($n = 3$). (c) GPx-like activity of hydrogels ($n = 3$). (d) Michaelis–Menten curves and Lineweaver–Burk plots of HCG@Cu/Zn-MOF at different GSH concentrations ($n = 3$), with nonlinear and double-reciprocal linear fitting. (e) TPx-like activity: cysteine depletion by hydrogels in the presence of H_2O_2 ($n = 3$). (f) APx-like activity: Ascorbic acid consumption by hydrogels in the presence of H_2O_2 ($n = 3$). (g) Michaelis–Menten curves and Lineweaver–Burk plots of HCG@Cu/Zn-MOF at different H2O2 concentrations ($n = 3$), with nonlinear and double-reciprocal linear fitting. (h) EPR spectra showing O_2^- elimination by HCG, HCG@ZIF-8, and HCG@Cu/Zn-MOF. (i) EPR spectra showing H_2O_2 elimination by HCG, HCG@ZIF-8, and HCG@Cu/Zn-MOF. All data are presented as mean ± SD. *ns* not significant; $^*P < 0.05$; $^{**}P < 0.01$; $^{***}P < 0.001$; $^{****}P < 0.0001$. One-way ANOVA and Tukey's post hoc test were performed to determine if the differences in the experimental data were statistically significant. *SD* standard deviation, SOD superoxide dismutase, *ZIF* zeolitic imidazolate framework, *EPR* electron paramagnetic resonance, *MOF* metal–organic framework, *ANOVA* analysis of variance, *HCG* hydroxypropyl methylcellulose chitosan glycerol

of residual GSH to produce a yellow product (2-nitro-5-thiobenzoic acid TNB) with absorbance at 412 nm. As shown in Figure 4c, all three HCG@Cu/Zn-MOF gels showed a marked decrease in absorbance relative to the absorbance of HCG and HCG@ZIF-8, indicating efficient GSH consumption and strong GPx-like activity. Similar to the SOD-like results, the HCG@3Cu/Zn-MOF group did not exhibit higher GPx-like activity than the HCG@2Cu/Zn-MOF group. Enzyme kinetics was calculated by varying GSH concentration and yielded a K_m of 2.52 mM and a V_{max} of 0.025 mM·min^{-1} (Figure 4d). The GPx-like activity of HCG@Cu/Zn-MOF was minimally affected by pH, with no significant absorbance changes observed between pH 5.5 and 8.5 (Figure S6b, see online supplementary material).

TPx is also an important peroxidase, and cysteine facilitates the reduction of H_2O_2 catalyzed by TPx to H_2O. We also used the assayed amount of generated TNB to assess the TPx-like characteristics of HCG@Cu/Zn-MOF. Figure 4e shows that cysteine depletion occurred more rapidly in hydrogels loaded with Cu/Zn-MOF nanoparticles than in the HCG and HCG@ZIF-8 groups, while the HCG@3Cu/Zn-MOF gel group did not exhibit higher TPx-like activity. The reaction environment was changed by adjusting the pH, and the TPx-like characteristics of HCG@Cu/Zn-MOF were greatly reduced in the alkaline environment relative to those in neutral and acidic settings (Figure S6c, see online supplementary material).

Another powerful peroxidase, APx, catalyzes the conversion of H_2O_2 to H_2O when AsA is present (Figure 4a). To evaluate the APx-like function of HCG@Cu/Zn-MOF, the absorption of AsA at 290 nm was measured over time. The absorbance of AsA decreased greatly when HCG@Cu/Zn-

Downloaded from academic.oup.com/burnstrauma/article/doi/10.1093/burnst/tkaf076/8341464 by guest on 12 October 2026

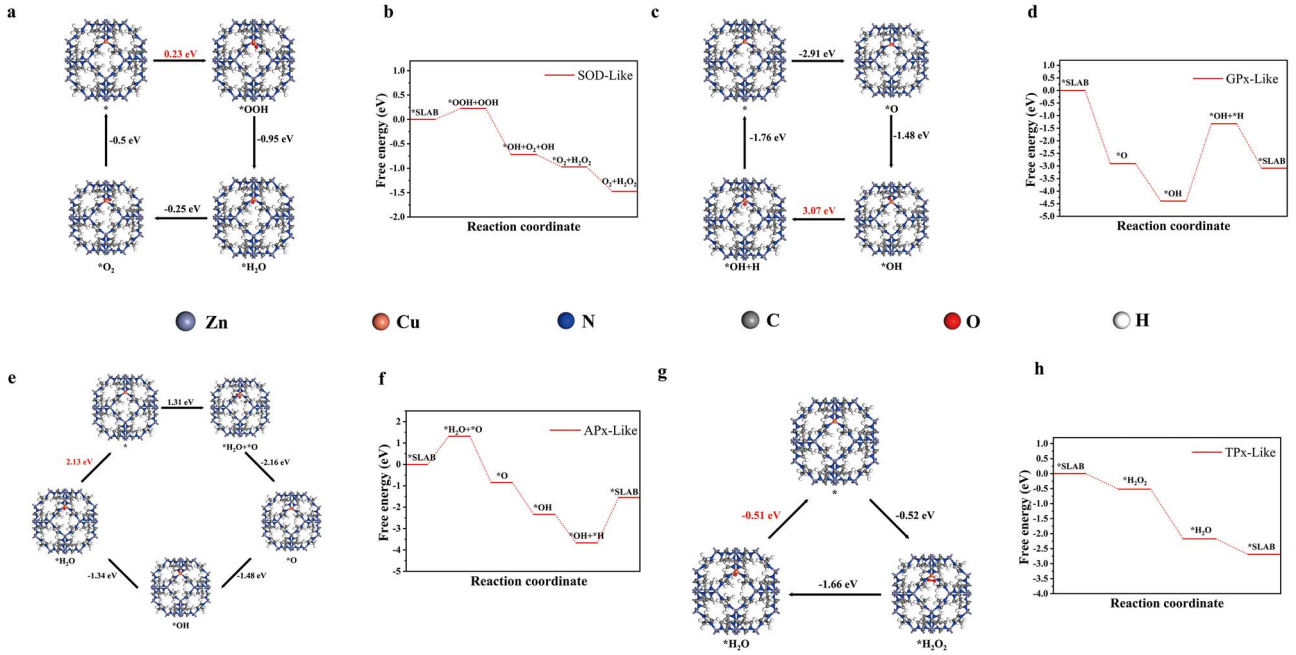


Figure 5. DFT investigation of four antioxidant enzyme-like mechanisms of HCG@Cu/Zn-MOF. (a) DFT-simulated pathways of SOD-like activities in HCG@Cu/Zn-MOF. (b) Free energy curve of SOD-like enzyme catalytic processes. (c) DFT-simulated pathways of GPx-like activities in HCG@Cu/Zn-MOF. (d) Free energy curve of GPx-like enzyme catalytic processes. (e) DFT-simulated pathways of APx-like activities in HCG@Cu/Zn-MOF. (f) Free energy curve of APx-like enzyme catalytic processes. (g) DFT-simulated pathways of TPx-like activities in HCG@Cu/Zn-MOF. (h) Free energy curve of TPx-like enzyme catalytic processes. *SD* standard deviation, *DFT* density functional theory, *SOD* superoxide dismutase, *ZIF* zeolitic imidazolate framework, *HCG* hydroxypropyl methylcellulose chitosan glycerol, *MOF* metal–organic framework

MOF hydrogel was added to the reaction, whereas the addition of HCG and HCG@ZIF-8 caused almost no change (Figure 4f). Consistent with the SOD, GPx, and TPx activities, no substantial change in APx-like activity was observed in the HCG@3Cu/Zn-MOF gel group compared with the HCG@2Cu/Zn-MOF gel group. The enzyme kinetic profile was calculated by varying the concentration of H_2O_2, giving a K_m of 2.13 mM and a V_{max} of 0.032 mM per min (Figure 4g). Furthermore, the APx-like activity of HCG@Cu/Zn-MOF was improved under acidic conditions relative to the activities under neutral and alkaline conditions (Figure S6d, see online supplementary material).

Since HCG@2Cu/Zn-MOF exhibited comparable enzyme-like activity to HCG@3Cu/Zn-MOF, O_2^- and H_2O_2 elimination by HCG@2Cu/Zn-MOF was further examined by EPR. As shown in Figure 4h, the HCG group displayed the highest signal intensity, indicating minimal O_2^- removal. The HCG@ZIF-8 group signal decreased, whereas the HCG@2Cu/Zn-MOF curve was nearly flat, indicating almost complete O_2^- elimination with superior efficiency. Time-resolved EPR further confirmed O_2^- elimination by HCG@2Cu/Zn-MOF, showing nearly complete removal within 15 min (Figure S7a, see online supplementary material). As shown in Figure 4i, H_2O_2 treated with HCG gels retained a distinct proton hyperfine structure, whereas treatment with HCG@2Cu/Zn-MOF markedly reduced this resolution, indicating strong scavenging capacity. Time-dependent analysis further revealed that H_2O_2 was largely eliminated within 15 min (Figure S7b, see online supplementary material).

In summary, HCG@2Cu/Zn-MOF demonstrated superior O_2^- removal capacity and efficiently consumed H_2O_2 through multiple pathways, which enhanced ROS scavenging. Since HCG@3Cu/Zn-MOF did not exhibit superior enzyme-like activity and showed some cytotoxicity in the CCK-8 assay (Figure S8, see online supplementary material), HCG@2Cu/Zn-MOF was selected for subsequent cellular and animal studies. For convenience, HCG@2Cu/Zn-MOF is hereafter referred to as HCG@Cu/Zn-MOF.

Density functional theory calculation

Experimental results confirmed that Cu/Zn-MOF exhibited catalytic activities analogous to SOD, GPx, TPx, and APx. To elucidate the underlying mechanisms, the four enzyme-like reactions of Cu/Zn-MOF were simulated using DFT. Figure 5a illustrates the SOD-like pathway, in which Cu sites initially adsorbed *OOH, the hydrated form of O_2^-. Decomposition of *OOH yielded *OH and adsorbed $*O_2$, followed by release of O_2 and H_2O_2. The calculated free-energy profile indicated a barrier of 0.23 eV (Figure 5b), suggesting a relatively fast reaction rate.

Figure 5c shows the GPx-like pathway, including (i) decomposition of H_2O_2 to yield H_2O and adsorbed *O, (ii) GSH decomposition to form adsorbed *OH and *H, and (iii) release of *OH and binding of *H to form H_2O. DFT calculations identified a critical adsorption step of *OH and *H with a free-energy barrier of 3.07 eV (Figure 5d).

The modeled APx-like pathway (Figure 5e) was similar to that of GPx, including (i) decomposition of H_2O_2 into $*H_2O$ and *O, (ii) release of $*H_2O$ to form H_2O, (iii) oxidation of AsA to monodehydroascorbate with formation of *OH and $*H_2O$, and (iv) desorption of $*H_2O$, producing H_2O. The rate-limiting step had a free-energy barrier of 2.13 eV (Figure 5f).

A potential TPx-like pathway was also modeled (Figure 5g). Cu/Zn-MOF initially adsorbed $*H_2O_2$, which subsequently decomposed upon reaction with cysteine, generating adsorbed

Downloaded from academic.oup.com/burnstrauma/article/doi/10.1093/burnst/tkaf076/8341464 by guest on 12 October 2026

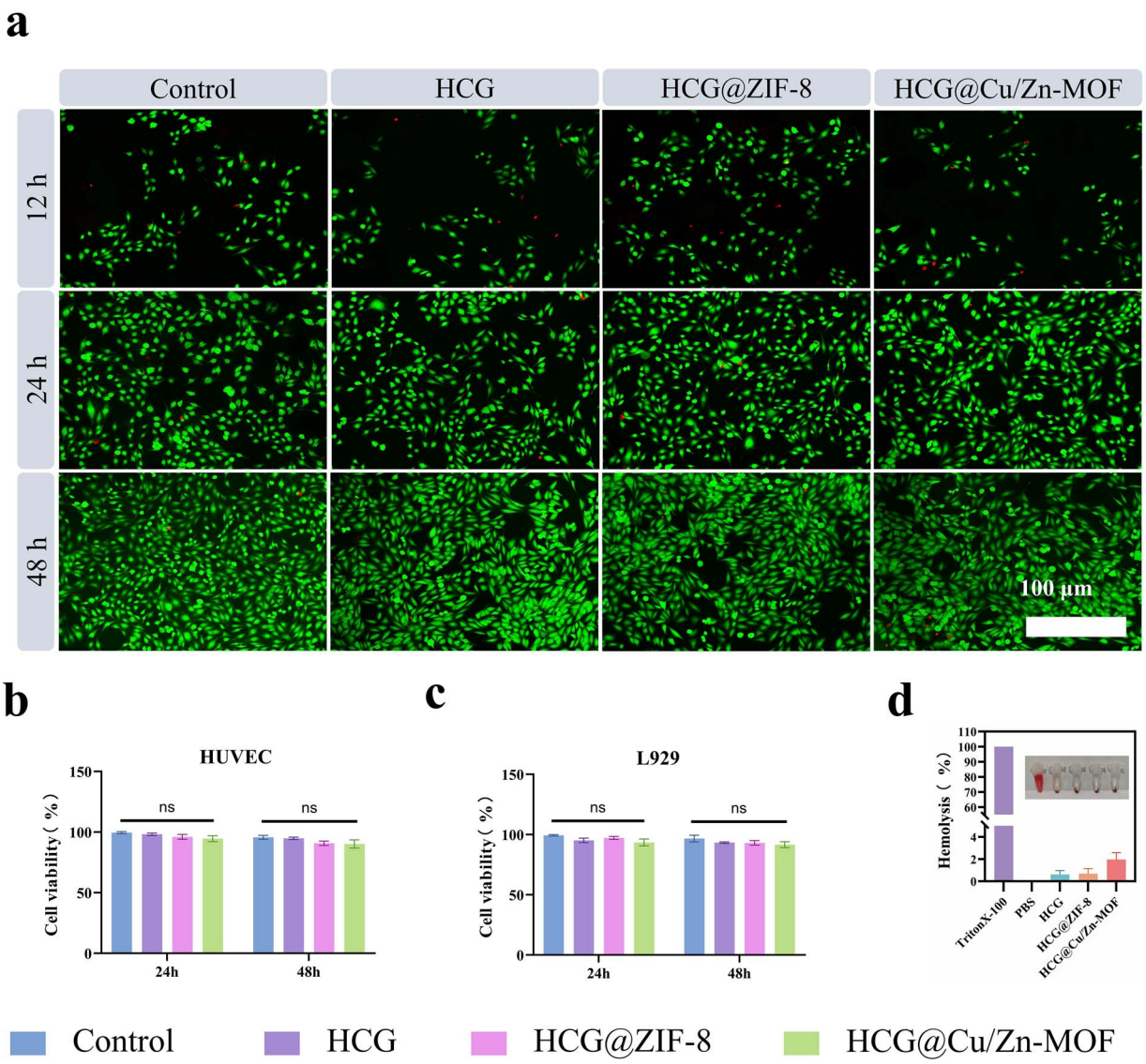


Figure 6. Biocompatibility of HCG@Cu/Zn-MOF hydrogel and its effects on cell proliferation and migration. (a) Fluorescence images of L929 cells stained with a live/dead kit after culture with hydrogel extracts. Scale bar : 100 μm. (b and c) OD values determined by performing the cell counting kit-8 assay after co-incubation of L929 and HUVEC cells with hydrogel extracts for 24 and 48 h ($n = 3$). (d) Hemolysis analysis of hydrogels ($n = 3$). All data are presented as mean ± SD. *ns* not significant; $^{*}P < 0.05$; $^{**}P < 0.01$; $^{***}P < 0.001$; $^{****}P < 0.0001$. Statistically significant differences in the experimental data were determined by performing two-way ANOVA and Tukey's post hoc test. *OD* optical density, *HUVECs* human umbilical vein endothelial cells, *SD* standard deviation, *MOF* metal–organic framework, *HCG* hydroxypropyl methylcellulose chitosan glycerol

$^{*}H_2O$ that was released to form H_2O. DFT calculations (Figure 5h) showed the lowest free-energy barrier (−0.51 eV), indicating that the TPx-like pathway was most favorable and that $^{*}H_2O$ was readily desorbed from the Cu/Zn-MOF.

In summary, DFT modeling of four enzyme-like pathways confirmed that Cu/Zn-MOF exhibited efficient antioxidant enzyme-mimicking activity for ROS scavenging.

In vitro biocompatibility of HCG@Cu/Zn-MOF

The biocompatibility of the hydrogels was evaluated by hemolysis and cytotoxicity assays. Fluorescence imaging revealed that most L929 cells cultured with extracts of HCG, HCG@ZIF-8, and HCG@Cu/Zn-MOF exhibited green fluorescence at 12, 24, and 48 h, whereas red fluorescence was rarely observed (Figure 6a). Cell viability of L929 and HUVEC cells after 24 and 48 h of culture was quantitatively assessed by performing the CCK-8 assay. In all groups, viability exceeded 90%, indicating excellent cytocompatibility (Figure 6b and c). In hemolysis assays, blood samples treated with PBS, HCG, HCG@ZIF-8, and HCG@Cu/Zn-MOF hydrogel extracts remained clear, whereas samples treated with Triton X-100 appeared red, indicating pronounced hemolysis. Quantitative analysis demonstrated that the hemolysis rates of the HCG, HCG@ZIF-8, and HCG@Cu/Zn-MOF hydrogels were all < 5%, indicating a low risk of hemolysis (Figure 6d). Collectively, these results confirmed that the HCG, HCG@ZIF-8, and HCG@Cu/Zn-MOF hydrogels possessed good biocompatibility.

HCG@Cu/Zn-MOF hydrogel promotes cell migration and angiogenesis

The potential of the hydrogels to enhance cell migration was investigated *in vitro*. As shown in Figure 7a, scratches in

Downloaded from academic.oup.com/burnstrauma/article/doi/10.1093/burnst/tkaf076/8341464 by guest on 12 October 2026

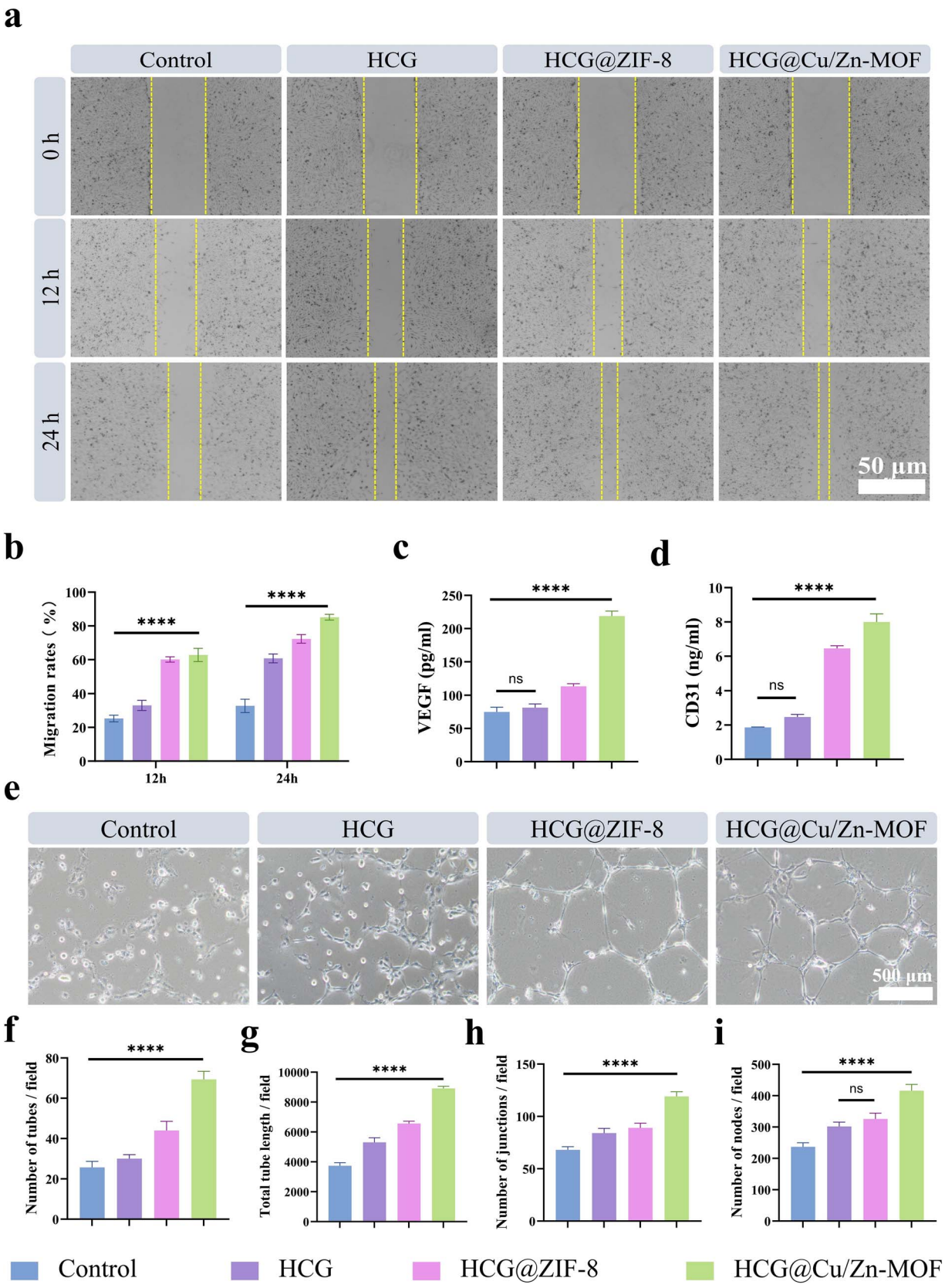


Figure 7. Effect of the HCG@Cu/Zn-MOF hydrogel on angiogenesis. (a) Migration images of L929 cells at 12 and 24 h after scratch assay. Scale bar: 50 μm. (b) Quantitative using ImageJ (n = 3) of the migrated area at 12 and 24 h. (c and d) VEGF and CD31 expression in HUVECs from different treatment groups, determined by ELISA (n = 3). (e) Representative angiogenesis images of HUVECs after incubation with hydrogel extracts. Scale bar = 500 μm. (f–i) Quantitative analysis of angiogenesis using ImageJ (n = 3). All data are presented as mean ± SD. *ns* not significant; $^{*}P < 0.05$; $^{**}P < 0.01$; $^{***}P < 0.001$; $^{****}P < 0.0001$. Statistically significant differences in experimental data were determined by one-way ANOVA and Tukey's post hoc test. *HUVECs* human umbilical vein endothelial cells, *SD* standard deviation, *MOF* metal–organic framework, *HCG* hydroxypropyl methylcellulose chitosan glycerol, *VEGF* vascular endothelial growth factor, *ELISA* enzyme-linked immunosorbent assay

Downloaded from academic.oup.com/burnstrauma/article/doi/10.1093/burnst/tkaf076/8341464 by guest on 12 October 2026

the cells treated with HCG@Cu/Zn-MOF extracts displayed significant closure after 12 h and almost complete closure after 24 h, whereas scratches in the control and HCG groups persisted. Quantitative analysis of the scratch area confirmed these findings (Figure 7b). A high-glucose microenvironment was simulated *in vitro*, and cells cultured in high-glucose medium were co-incubated with hydrogels to assess migration. As shown in Figure S9, scratches in cells treated with HCG@Cu/Zn-MOF were nearly closed after 24 h, indicating enhanced migration-promoting effects. These results suggest that ion release from HCG@Cu/Zn-MOF hydrogels facilitates cell migration.

To evaluate neovascularization, angiogenesis-related proteins, including VEGF and CD31, were assessed [47, 48]. VEGF and CD31 expression levels were quantified by performing an enzyme-linked immunosorbent assay (ELISA) after 24 h of co-incubation of HUVECs with hydrogel extracts. The HCG@Cu/Zn-MOF group exhibited markedly higher VEGF and CD31 expression than that of the control group (Figure 7c and d). Furthermore, angiogenesis assays were conducted to evaluate the pro-angiogenic potential of the hydrogels. As shown in Figure 7e, HCG@Cu/Zn-MOF significantly enhanced angiogenesis. HUVECs treated with HCG@Cu/Zn-MOF formed more neovessels, branches, junctions, and longer vessel lengths compared with controls (Figure 7f–i).

Collectively, these results indicate that the HCG@Cu/Zn-MOF hydrogels possess good biocompatibility and effectively promote cell migration and angiogenesis, thereby supporting accelerated wound healing.

In vitro reactive oxygen species scavenging and anti-inflammatory capacity

To evaluate the protective effects of HCG@Cu/Zn-MOF hydrogels, oxidative stress was induced in L929 cells (Figure 8a). ROS levels were assessed using DCFH-DA and Hoechst staining following an LPS-induced ROS burst. Control cells showed minimal green fluorescence, whereas LPS-treated cells showed strong green fluorescence, indicating ROS accumulation. Treatment with HCG gel did not attenuate fluorescence, whereas HCG@ZIF-8 produced a modest reduction. In contrast, HCG@Cu/Zn-MOF markedly reduced green fluorescence (Figure 8b). Quantitative analysis confirmed these findings, as did flow cytometry (Figure 8c and d).

Pro-inflammatory and anti-inflammatory cytokine expression was evaluated by ELISA across treatment groups. As shown in Figure 8e, LPS induced substantial overproduction of TNF-α, IL-1β, and IL-33 (492.34, 461.49, and 183.99 pg/ml, respectively). HCG gel had no significant effect, whereas HCG@ZIF-8 moderately reduced cytokine levels to 277.34, 309.56, and 120.37 pg/ml, respectively. In contrast, HCG@Cu/Zn-MOF markedly reduced TNF-α, IL-1β, and IL-33 to 119.88, 117.43, and 61.59 pg/ml by ~75%. Notably, HCG@Cu/Zn-MOF also significantly increased anti-inflammatory cytokine release (Figure 8f). IL-10 and IL-4 levels increased from 21.16 and 15.79 pg/ml (LPS group) to 120.17 and 161.53 pg/ml, respectively, after treatment.

To investigate the underlying mechanisms, protein expression was analyzed by western blot. Under oxidative stress, ROS act as inflammatory triggers that activate the NF-κB pathway. Activated NF-κB translocates to the nucleus, binds promoter regions, and upregulates pro-inflammatory genes, amplifying the cascade [49, 50]. Sirt1, an upstream regulator of NF-κB, modulates its activity through deacetylation [51]. As shown in Figure 8g–i, LPS-stimulated L929 cells exhibited strong oxidative stress and NF-κB activation, resulting in nuclear translocation, increased pro-inflammatory factor expression, and amplified inflammation, but Sirt1 expression was suppressed. HCG@ZIF-8 modestly promoted Sirt1 expression and inhibited NF-κB, but the effects were limited. In contrast, HCG@Cu/Zn-MOF significantly increased Sirt1 expression, interacted with the NF-κB p65 subunit, and suppressed NF-κB activity through deacetylation. Collectively, these findings demonstrate that HCG@Cu/Zn-MOF exerts potent anti-inflammatory effects by upregulating Sirt1, suppressing NF-κB, and modulating downstream pro-inflammatory and anti-inflammatory cytokines.

Anti-apoptotic ability *in vitro*

Since ROS accumulation decreases $\Delta\Psi$m and promotes apoptosis, the protective effect of the HCG@Cu/Zn-MOF hydrogels against apoptosis was further evaluated. Experiments were conducted on normal HUVECs and those cultured in high-glucose medium. To assess $\Delta\Psi$m, JC-10 staining (red/green fluorescence) was performed, and apoptosis was quantified by flow cytometry. The results are shown in Figure 9a. The control cells displayed predominantly red fluorescence with minimal green signal, indicating intact mitochondrial function. Treatment with LPS markedly increased green fluorescence, confirming $\Delta\Psi$m loss. The HCG hydrogel did not alter the red/green ratio, indicating no therapeutic effect. Both HCG@ZIF-8 and HCG@Cu/Zn-MOF reduced green fluorescence, which was stronger in the HCG@Cu/Zn-MOF group. Quantitative red/green fluorescence analysis (Figure 9b) confirmed that HCG@Cu/Zn-MOF stabilized $\Delta\Psi$m. Similar results were observed in HUVECs cultured under high-glucose conditions, where HCG@Cu/Zn-MOF provided superior $\Delta\Psi$m protection and reduced apoptosis (Figure S10a and b, see online supplementary material).

Anti-apoptotic effects were also quantified by flow cytometry (Figure 9c and d). The proportion of Annexin V/PI-positive cells was significantly lower in the HCG@Cu/Zn-MOF group than in the LPS group, indicating reduced apoptosis. This effect was also confirmed in high-glucose–treated cells (Figure S10c and d, see online supplementary material). Collectively, these findings demonstrate that HCG@Cu/Zn-MOF hydrogels protect against ROS-induced apoptosis.

In vitro bacterial inhibition assay

In addition to oxidative stress, bacterial infection is a major factor that hinders diabetic wound healing. Among pathogenic species, *E. coli* and *S. aureus* are the most common culprits; therefore, the antibacterial activity of the HCG@Cu/Zn-MOF hydrogels was evaluated. As shown in Figure 10a–c, the HCG hydrogel exhibited modest antibacterial activity, likely due to the positive surface charge of CS, but failed to effectively kill bacteria. Incorporation of ZIF-8 into HCG enhanced antimicrobial activity through sustained Zn^{2+} release, achieving killing rates of 49.7% against *E. coli* and 41.65% against *S. aureus*. The HCG@Cu/Zn-MOF group demonstrated the strongest antibacterial effect, with synergistic contributions from Cu^{2+}, Zn^{2+}, and CS, achieving

Downloaded from academic.oup.com/burnstrauma/article/doi/10.1093/burnst/tkaf076/8341464 by guest on 12 October 2026

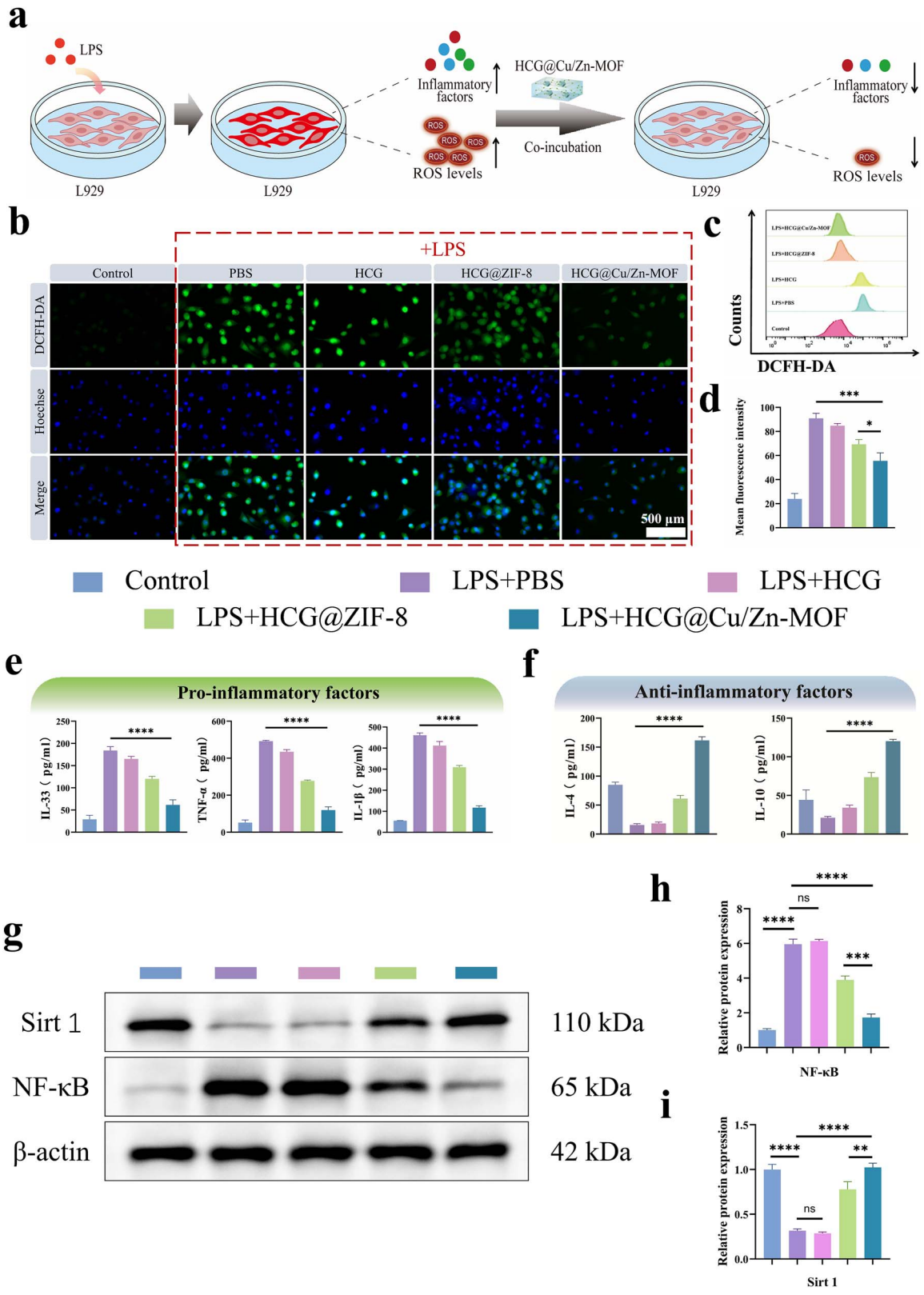


Figure 8. ROS-scavenging and anti-inflammatory properties of the HCG@Cu/Zn-MOF hydrogels. (a) Schematic illustration of HCG@Cu/Zn-MOF hydrogel for ROS scavenging and inflammation reduction. (b) Fluorescence images obtained from a DCFH-DA probe of ROS in L929 cells treated with different materials are shown. Scale bar: 500 μm. (c) Flow cytometry analysis of ROS levels in DCFH-DA-stained L929 cells treated with different materials. (d) Quantitative analysis of fluorescence intensity in L929 cells ($n = 3$). (e) ELISA measurement of pro-inflammatory factors (IL-33, TNF-α, and IL-1β) in L929 cells after treatment with different hydrogels ($n = 3$). (f) ELISA measurement of anti-inflammatory factors (IL-4 and IL-10) in L929 cells after treatment with different hydrogels ($n = 3$). (g) Western blot analysis of NF-κB and Sirt1 expression. (h, i) quantitative analysis of NF-κB and Sirt1 expression ($n = 3$). All data are presented as mean ± SD. *ns* not significant; $^{*}P < 0.05$; $^{**}P < 0.01$; $^{***}P < 0.001$; $^{****}P < 0.0001$. Statistically significant differences in experimental data were determined by performing one-way ANOVA and Tukey's post hoc test. *ROS* reactive oxygen species, *HUVECs* human umbilical vein endothelial cells, *SD* standard deviation, *MOF* metal–organic framework, *HCG* hydroxypropyl methylcellulose chitosan glycerol, *VEGF* vascular endothelial growth factor, *ELISA* enzyme-linked immunosorbent assay, *NF-κB* nuclear factor-κ beta, *IL* interleukin, *TNF* tumor necrosis factor, *ANOVA* analysis of variance

Downloaded from academic.oup.com/burnstrauma/article/doi/10.1093/burnst/tkaf076/8341464 by guest on 12 October 2026

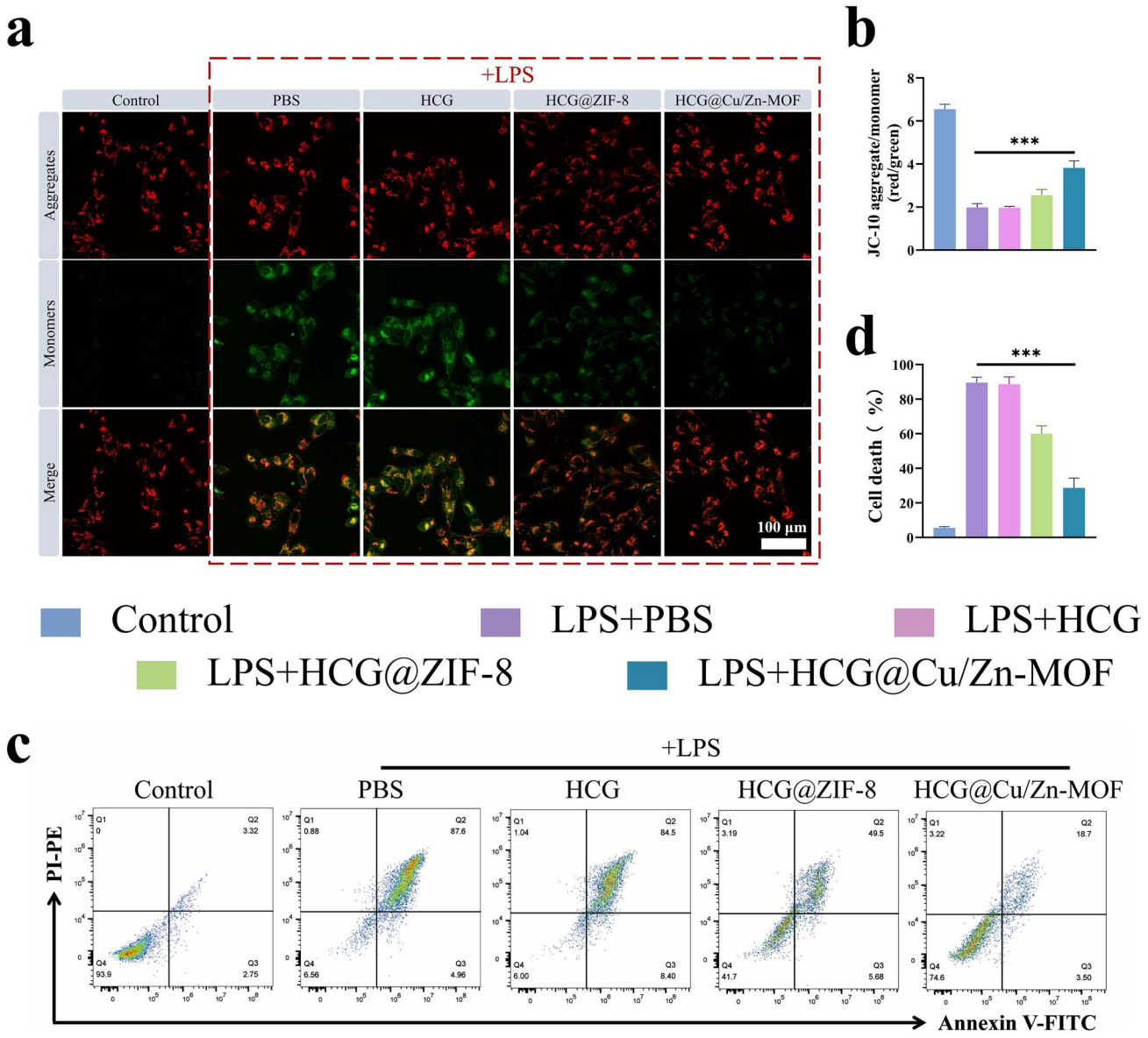


Figure 9. Anti-apoptotic effects of the HCG@Cu/Zn-MOF hydrogel in HUVECS. (a) Detection of mitochondrial membrane potential ($\Delta\Psi$m) by JC-10 staining after treatment of the HUVECs with different materials (Scale bar: 100 μm). (b) Quantitative analysis of the red/green fluorescence ratio with ImageJ software ($n = 3$). (c) Flow cytometry analysis of Annexin V-FITC/PI double staining in HUVECs. (d) Quantitative analysis of apoptotic cell percentages by flow cytometry ($n = 3$). All data are presented as mean ± SD. *ns* not significant; $^{*}P < 0.05$; $^{**}P < 0.01$; $^{***}P < 0.001$; $^{****}P < 0.0001$. Statistically significant differences in the experimental data were determined by performing one-way analysis of variance and Tukey's post hoctest. *HUVECs* human umbilical vein endothelial cells, *SD* standard deviation, *MOF* metal–organic framework, *HCG* hydroxypropyl methylcellulose chitosan glycerol

killing rates of 99.39% against *E. coli* and 99.67% against *S. aureus*. These results were further confirmed by bacterial live/dead staining. As shown in Figure 10d and e, HCG-treated bacteria remained largely green (viable), with minimal red fluorescence. HCG@ZIF-8 treatment increased red fluorescence, but a substantial green signal persisted, indicating incomplete killing. In contrast, HCG@Cu/Zn-MOF treatment nearly eliminated green fluorescence while markedly increasing red fluorescence, confirming bactericidal efficacy consistent with plate-count results. Bacterial morphological changes were examined by SEM (Figure 10f). Most bacteria treated with HCG retained intact morphology. HCG@ZIF-8 caused partial damage, including wall rupture, wrinkling, and membrane shrinkage. In contrast, HCG@Cu/Zn-MOF treatment induced severe structural disruption, with complete wall rupture, membrane collapse, and leakage of intracellular components, demonstrating potent antibacterial activity. In summary, HCG@Cu/Zn-MOF hydrogels not only provided strong antioxidant protection but also exhibited excellent bactericidal capacity, highlighting their synergistic benefits for promoting diabetic wound healing.

Hydrogels for diabetic infected wound repair *in vivo*

The therapeutic effects of hydrogels on wound repair were evaluated using a full-thickness wound model in diabetic mice. After establishing the diabetic mouse model (Figure S11, see online supplementary material), the mice were randomly

Downloaded from academic.oup.com/burnstrauma/article/doi/10.1093/burnst/tkaf076/8341464 by guest on 12 October 2026

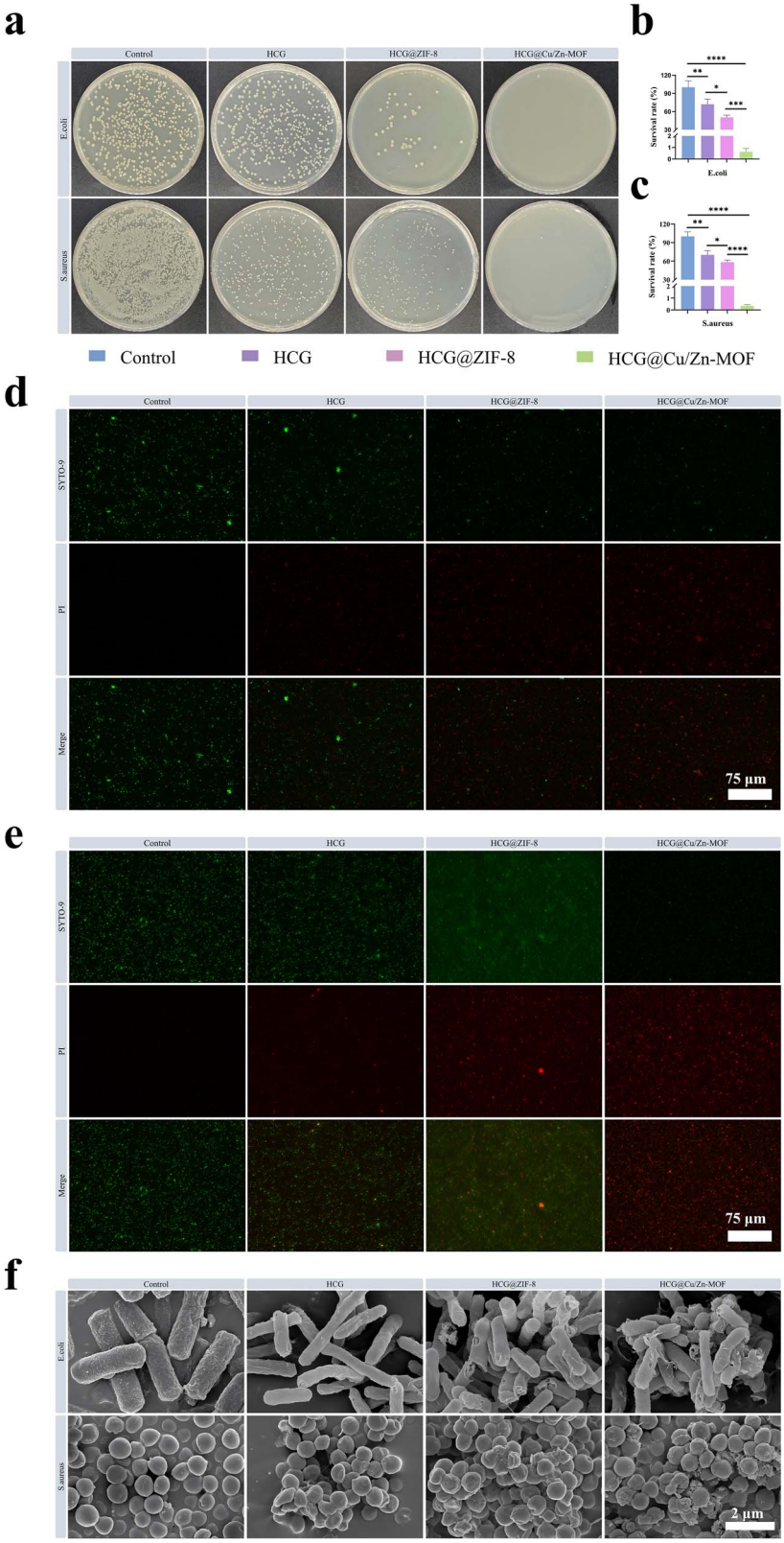


Figure 10. Antimicrobial properties of the HCG@Cu/Zn-MOF hydrogels. (a–c) Representative plate images and bacterial survival after treatment of *S. aureus* and *E. coli* with hydrogels ($n = 3$). (d and e) Live/dead staining of *E. coli* and *S. aureus*; red fluorescence indicates dead cells. Scale bar: 75 μm. (f) Scanning electron microscopy images showing morphological changes in *E. coli* and *S. aureus* after hydrogel treatment. Scale bar: 2 μm. All data are presented as mean ± SD. *ns* not significant; $^{*}P < 0.05$; $^{**}P < 0.01$; $^{***}P < 0.001$; $^{****}P < 0.0001$. Statistically significant differences in the experimental data were determined by performing one-way analysis of variance and Tukey's post hoc test. *HUVECs* human umbilical vein endothelial cells, *SD* standard deviation, *MOF* metal–organic framework, *HCG* hydroxypropyl methylcellulose chitosan glycerol, *E. coli Escherichia coli*, *S. aureus Staphylococcus aureus*

Downloaded from academic.oup.com/burnstrauma/article/doi/10.1093/burnst/tkaf076/8341464 by guest on 12 October 2026

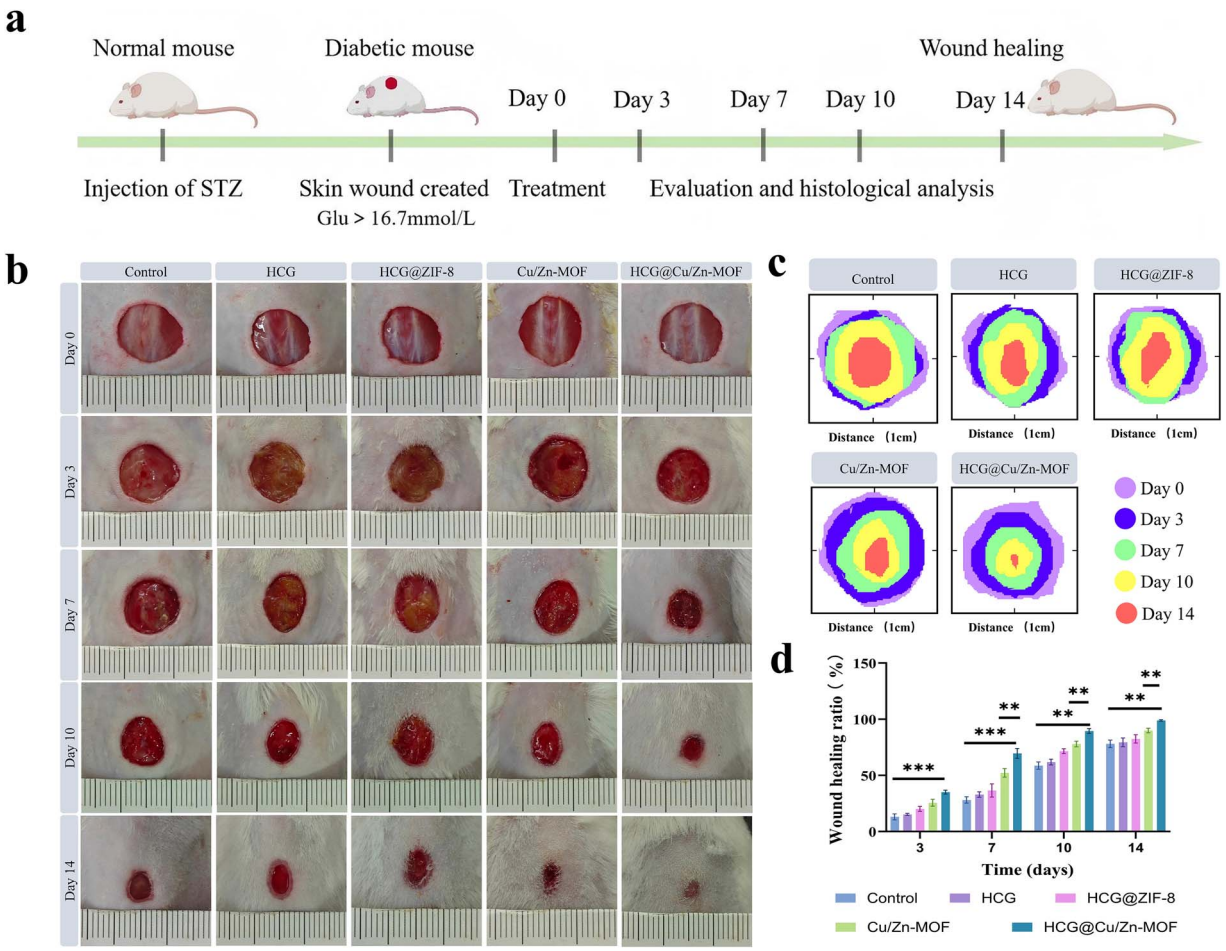


Figure 11. Therapeutic efficacy of the HCG@Cu/Zn-MOF hydrogel in a full-thickness wound model in diabetic mice. (a) Schematic timeline of animal model establishment and hydrogel treatment in diabetic mice. (b) Representative wound images on days 0, 3, 7, 10, and 14 after treatment with different materials. (c) Tracing of wound-bed closure in different groups on day 14. (d) Quantitative wound closure rates of different groups at day 14 ($n = 3$). All data are presented as mean ± SD. *ns* not significant; $^{*}P < 0.05$; $^{**}P < 0.01$; $^{***}P < 0.001$; $^{****}P < 0.0001$. Statistically significant differences in the experimental data were determined by performing two-way ANOVA and Tukey's post hoc test. *SD* standard deviation, *MOF* metal–organic framework, *HCG* hydroxypropyl methylcellulose chitosan glycerol, *ANOVA* analysis of variance

assigned to five treatment groups. Full-thickness circular wounds were created and treated with saline (control), HCG gel, HCG@ZIF-8 gel, Cu/Zn-MOF, or HCG@Cu/Zn-MOF gel. At predetermined time points, wound size was recorded, and tissue samples were collected for H&E and Masson's trichrome staining (Figure 11a).

As shown in Figure 11b and c, wound size was monitored on days 3, 7, 10, and 14, and relative wound closure rates were calculated to evaluate the extent of healing in each group (Figure 11d). On day 3, the control group showed the lowest closure rate (13.05%), whereas the HCG gel group showed no significant improvement (15.23%). The HCG@ZIF-8 group achieved a closure rate that was 7.08% higher than that of the controls, the Cu/Zn-MOF group reached 25.62%, and the HCG@Cu/Zn-MOF group demonstrated the best effect, with a 35.06% closure rate. By day 7, all groups showed wound reduction but to varying extents. Closure rates in the control, HCG, and HCG@ZIF-8 groups were similar (28.9%, 32.9%, and 35.5%, respectively). The Cu/Zn-MOF group showed enhanced healing with 52.24% closure, but the HCG@Cu/Zn-MOF group again showed superior performance with 69.56% closure. By day 10, wounds in the HCG@Cu/Zn-MOF group were nearly closed (89.49%), whereas residual wound areas remained in the control (41.33%), HCG (38.13%), HCG@ZIF-8 (28.41%), and Cu/Zn-MOF (22.03%) groups. By day 14, wound reduction was evident in all groups. Notably, the HCG@Cu/Zn-MOF group achieved nearly complete closure (98.89%), outperforming the control (78.08%), HCG (79.40%), HCG@ZIF-8 (82.49%), and Cu/Zn-MOF (89.95%) groups. These findings indicate that Cu/Zn-MOF accelerated wound healing compared with HCG and HCG@ZIF-8, probably due to Cu-induced antioxidative activity. However, its efficacy was limited by rapid ion release and loss at the wound surface. In contrast, the HCG@Cu/Zn-MOF hydrogel demonstrated the most effective wound healing because the HCG matrix enabled sustained release of Cu/Zn-MOF, providing prolonged activity and superior therapeutic outcomes.

Wound tissues were collected on days 7 and 14 for H&E and Masson's trichrome staining to assess histological changes. Granulation tissue regeneration, a recognized marker of wound healing, was evaluated [52]. As shown in Figure 12a and b, on day 7, the control, HCG, HCG@ZIF-8, and Cu/Zn-MOF groups exhibited sparsely arranged granulation tissue, whereas the HCG@Cu/Zn-MOF group

Downloaded from academic.oup.com/burnstrauma/article/doi/10.1093/burnst/tkaf076/8341464 by guest on 12 October 2026

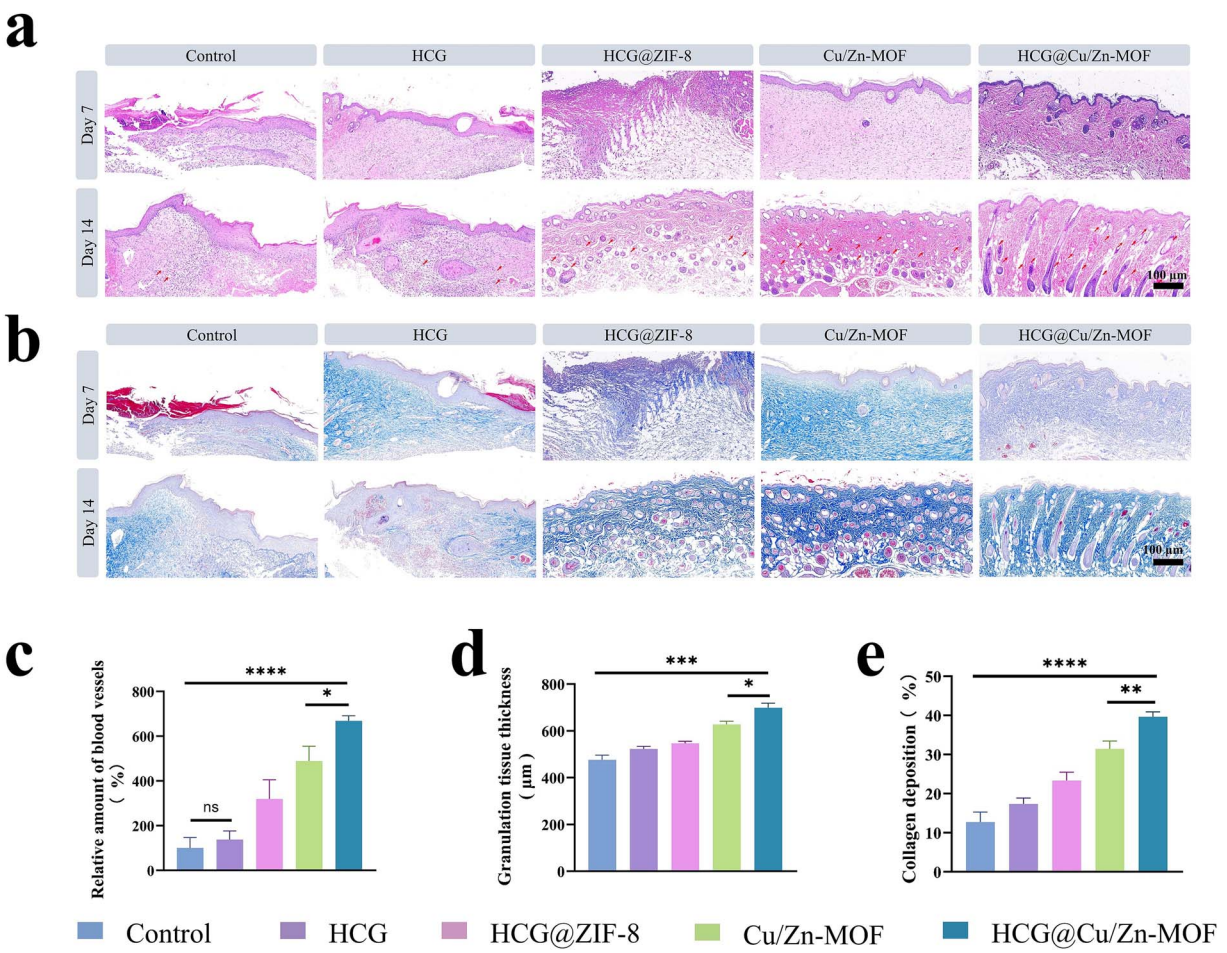


Figure 12. Histological evaluation of wound tissues at different time points. (a and b) Hematoxylin and eosin and Masson's trichrome staining of wound tissues on days 7 and 14 (red arrows indicate neovascularization). Scale bar: 100 μm. (c–e) Quantitative analysis of neovascularization, granulation tissue thickness, and collagen deposition in wound tissues ($n = 3$). All data are presented as mean ± SD. *ns* not significant; $^{*}P < 0.05$; $^{**}P < 0.01$; $^{***}P < 0.001$; $^{****}P < 0.0001$. Statistically significant differences in the experimental data were determined by performing one-way ANOVA and Tukey's post hoc test. *SD* standard deviation, *ANOVA* analysis of variance

exhibited markedly enhanced regeneration. By day 14, the HCG@Cu/Zn-MOF group showed the greatest regenerative effect, with granulation tissue thickness increases of 46.74%, 33.65%, 27.78%, and 11.84% relative to the control, HCG, HCG@ZIF-8, and Cu/Zn-MOF groups, respectively. The HCG@Cu/Zn-MOF group also exhibited strong pro-angiogenic activity, with neovascularization reaching 668% that of the control group (Figure 12c and d). Masson's staining further revealed greater collagen deposition in the HCG@Cu/Zn-MOF group on day 7 along with visible hair follicles and sebaceous glands. By day 14, wounds in this group exhibited densely packed collagen fibers, with collagen deposition reaching 39.6%, significantly higher than the control (12.73%), HCG (17.36%), HCG@ZIF-8 (23.35%), and Cu/Zn-MOF (31.43%) groups (Figure 12e). Moreover, numerous hair follicles were observed in the newly formed tissue, which were arranged in a regular pattern. These findings demonstrate the ability of HCG@Cu/Zn-MOF to accelerate diabetic wound repair by promoting granulation-tissue formation, angiogenesis, collagen deposition, and regeneration of skin appendages.

In diabetic wounds, ROS levels remain elevated, impairing vascular endothelial cell regeneration and angiogenesis. Therefore, immunofluorescence staining was performed to assess the antioxidant and pro-angiogenic effects of the HCG@Cu/Zn-MOF hydrogel in wound tissues. DHE staining was first used to assess ROS levels in wound tissues on day 14. Strong red fluorescence was observed in the control and HCG groups, indicating high ROS levels. Fluorescence intensity decreased following HCG@ZIF-8 treatment but remained apparent and was further reduced with Cu/Zn-MOF, although ROS persisted. In contrast, red fluorescence was nearly absent in the HCG@Cu/Zn-MOF group, demonstrating effective ROS clearance (Figure 13a). This finding reaffirmed the potent antioxidative ability of the HCG@Cu/Zn-MOF hydrogel, further confirmed by quantitative analysis of the ROS levels (Figure 13b). As oxidative stress subsided, wounds progressed to the remodeling phase, during which angiogenesis in granulation tissue became critical. This was evaluated by CD31 and VEGF expression. As shown in Figure 13c–f, HCG@Cu/Zn-MOF significantly upregulated VEGF and CD31 expression in regenerated skin after 14 days. Quantitative fluorescence analysis revealed that VEGF and CD31 increased by 394.8% and 381.64%, respectively, in the HCG@Cu/Zn-MOF group compared with the control, consistent with the *in vitro* results. To further investigate the anti-inflammatory mechanism of HCG@Cu/Zn-MOF *in vivo*, wound tissues were analyzed by western blot (Figure 13g–i). In STZ-induced diabetic mice, NF-κB expression was markedly elevated, whereas Sirt1 expression

Downloaded from academic.oup.com/burnstrauma/article/doi/10.1093/burnst/tkaf076/8341464 by guest on 12 October 2026

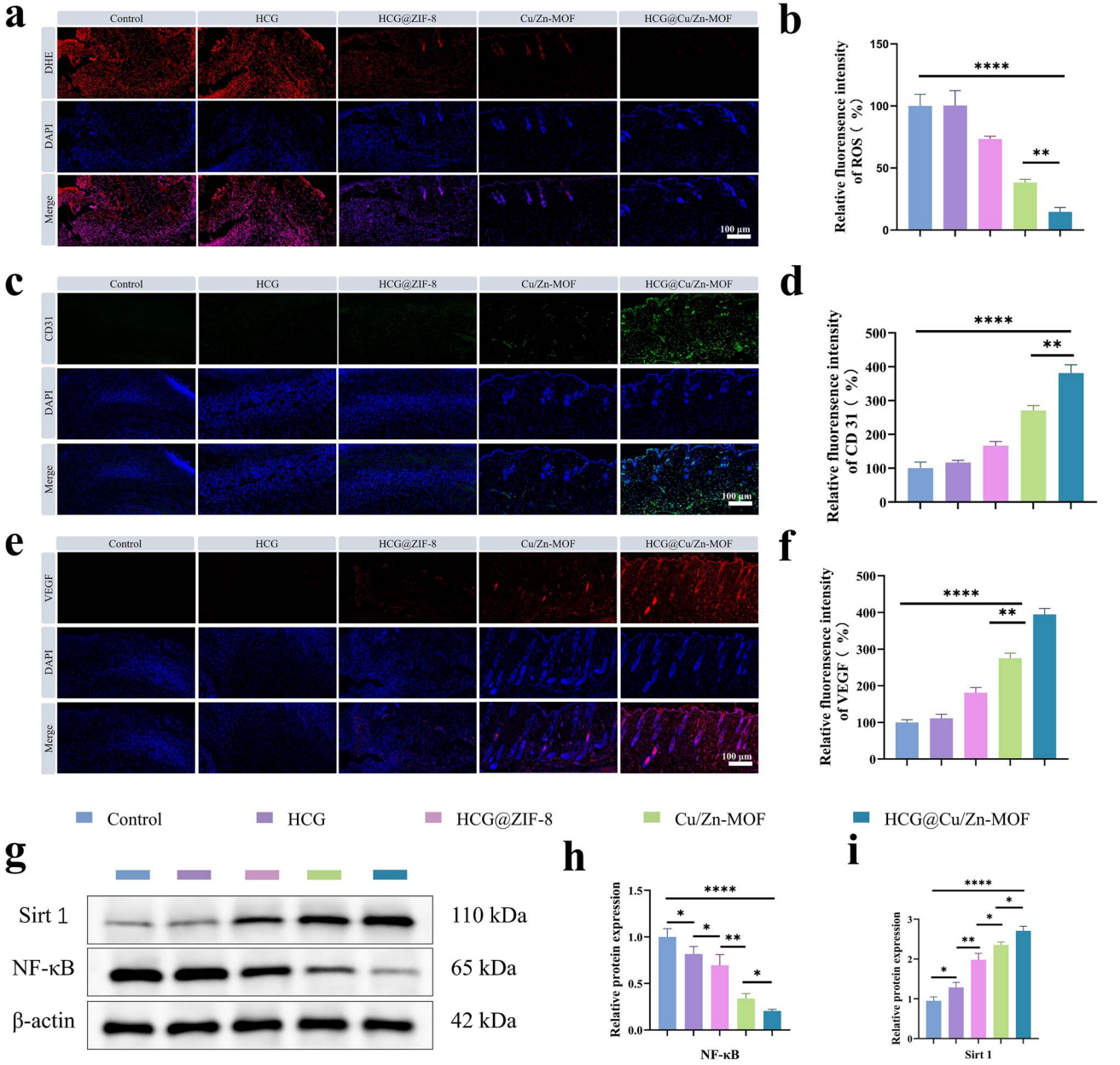


Figure 13. Pro-angiogenic and reactive oxygen species-scavenging effects of the HCG@Cu/Zn-MOF hydrogel in wounds. (a) Immunofluorescence staining of DHE in regenerated skin on day 14. Scale bar: 100 μm. (b) Quantitative analysis of DHE immunofluorescence (n = 3). (c) Immunofluorescence staining of CD31 in regenerated skin on day 14. Scale bar: 100 μm. (d) Quantitative analysis of CD31 immunofluorescence (n = 3). (e) Immunofluorescence staining of VEGF in regenerated skin on day 14. Scale bar: 100 μm. (f) Quantitative analysis of VEGF immunofluorescence (n = 3). (g) Western blot analysis of NF-κB and Sirt1 expression in mouse-wound tissues. (h and i) Quantitative analysis of NF-κB and Sirt1 expression (n = 3). All data are presented as mean ± SD. *ns* not significant; $^{*}P < 0.05$; $^{**}P < 0.01$; $^{***}P < 0.001$; $^{****}P < 0.0001$. Statistically significant differences in the experimental data were determined by performing one-way ANOVA and Tukey's post hoc test. *SD* standard deviation, *MOF* metal–organic framework, *HCG* hydroxypropyl methylcellulose chitosan glycerol, *ANOVA* analysis of variance, *VEGF* vascular endothelial growth factor, *DHE* dihydroethidium, *NF-κB* nuclear factor-κ beta

was suppressed. After HCG@Cu/Zn-MOF treatment, ROS clearance inhibited NF-κB activation and nuclear translocation, significantly reducing NF-κB expression. Concurrently, Sirt1 expression was upregulated, further suppressing NF-κB activity.

To evaluate the pro-healing effect of hydrogels on diabetic infected wounds, *S. aureus* suspension was applied to wounds in diabetic mice to establish an infected-wound model (Figure 14a). As shown in Figure 14b–d, the HCG and HCG@ZIF-8 groups exhibited limited healing capacity, with substantial unhealed areas still evident at day 14. The Cu/Zn-MOF group showed partial healing, although residual unhealed regions persisted. In contrast, the HCG@Cu/Zn-MOF group demonstrated the most pronounced healing, with wounds nearly closed, attributable to the sustained delivery and slow-release effect of the hydrogel. On day 3, bacterial culture of wound tissues revealed that the HCG@Cu/Zn-MOF group exhibited the strongest antimicrobial activity, achieving 97.98% bacterial mortality. This shortened infection duration, reduced infection-induced oxidative stress, and promoted efficient wound healing (Figure 14e and f). Furthermore, H&E and Masson's staining

Downloaded from academic.oup.com/burnstrauma/article/doi/10.1093/burnst/tkaf076/8341464 by guest on 12 October 2026

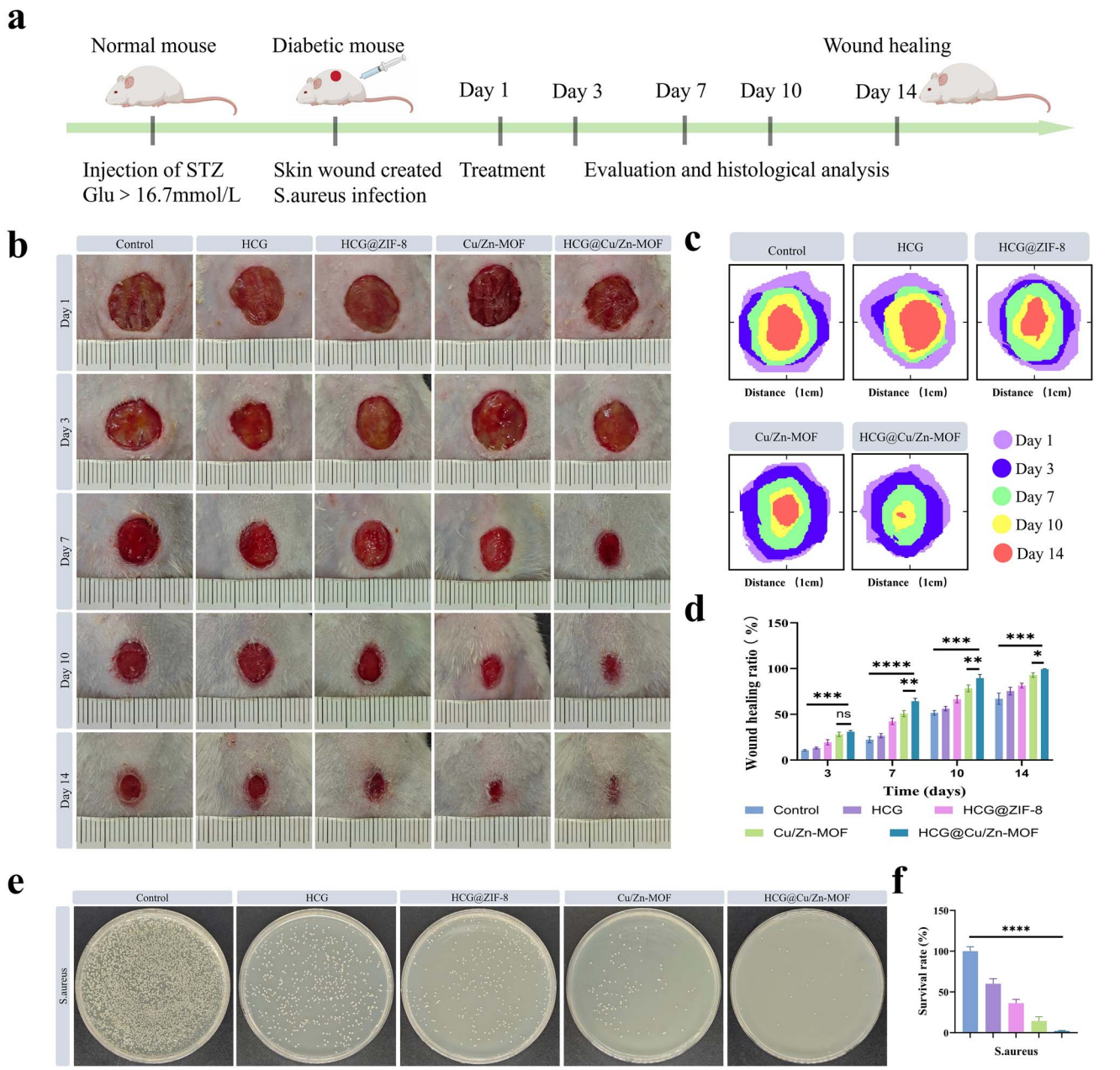


Figure 14. Therapeutic efficacy of HCG@Cu/Zn-MOF hydrogel in a full-thickness infected-wound model in diabetic mice. (a) Schematic timeline of animal model establishment and hydrogel treatment in diabetic mice with infected wounds. (b) Representative images of infected wounds on days 1, 3, 7, 10, and 14 after treatment with different materials. (c) Tracing of wound-bed closure in different groups on day 14. (d) Quantitative closure rates of infected wounds in different groups on day 14 ($n = 3$). (e and f) Bacterial plate counts and quantitative analysis of bacterial survival 3 days after hydrogel treatment ($n = 3$). All data are presented as mean ± SD. *ns* not significant; $^{*}P < 0.05$; $^{**}P < 0.01$; $^{***}P < 0.001$; $^{****}P < 0.0001$. Statistically significant differences in the experimental data were identified by performing one-way ANOVA, two-way ANOVA analysis, and Tukey's post hoc tests. *SD* standard deviation, *MOF* metal–organic framework, *HCG* hydroxypropyl methylcellulose chitosan glycerol, *ANOVA* analysis of variance

at days 7 and 14 confirmed the pro-healing effects of HCG@Cu/Zn-MOF (Figure 15a and b). On day 14, H&E staining revealed normal granulation-tissue formation and extensive neovascularization, whereas Masson's staining demonstrated substantial collagen deposition. Quantitative analysis confirmed significantly greater granulation tissue thickness, neovascular density, and collagen deposition in the HCG@Cu/Zn-MOF group compared with other groups (Figure 15c–e). Furthermore, immunofluorescence demonstrated the ROS-scavenging capacity of HCG@Cu/Zn-MOF in infected wounds. As shown in Figure 16a and b, red fluorescence in HCG@Cu/Zn-MOF-treated wounds was nearly absent, indicating effective ROS elimination. Furthermore, CD31 and VEGF expressions were significantly upregulated (Figure 16c-f), confirming enhanced angiogenesis and accelerated healing in infected wounds. Overall, HCG@Cu/Zn-MOF hydrogel exhibited robust pro-healing activity in diabetic infected wounds by combining antimicrobial and ROS-scavenging effects, thereby promoting granulation-tissue formation, vascular regeneration, and collagen deposition.

Finally, to evaluate the *in vivo* biocompatibility of the HCG@Cu/Zn-MOF hydrogel, body-weight changes were monitored throughout the treatment period. Routine

Downloaded from academic.oup.com/burnstrauma/article/doi/10.1093/burnst/tkaf076/8341464 by guest on 12 October 2026

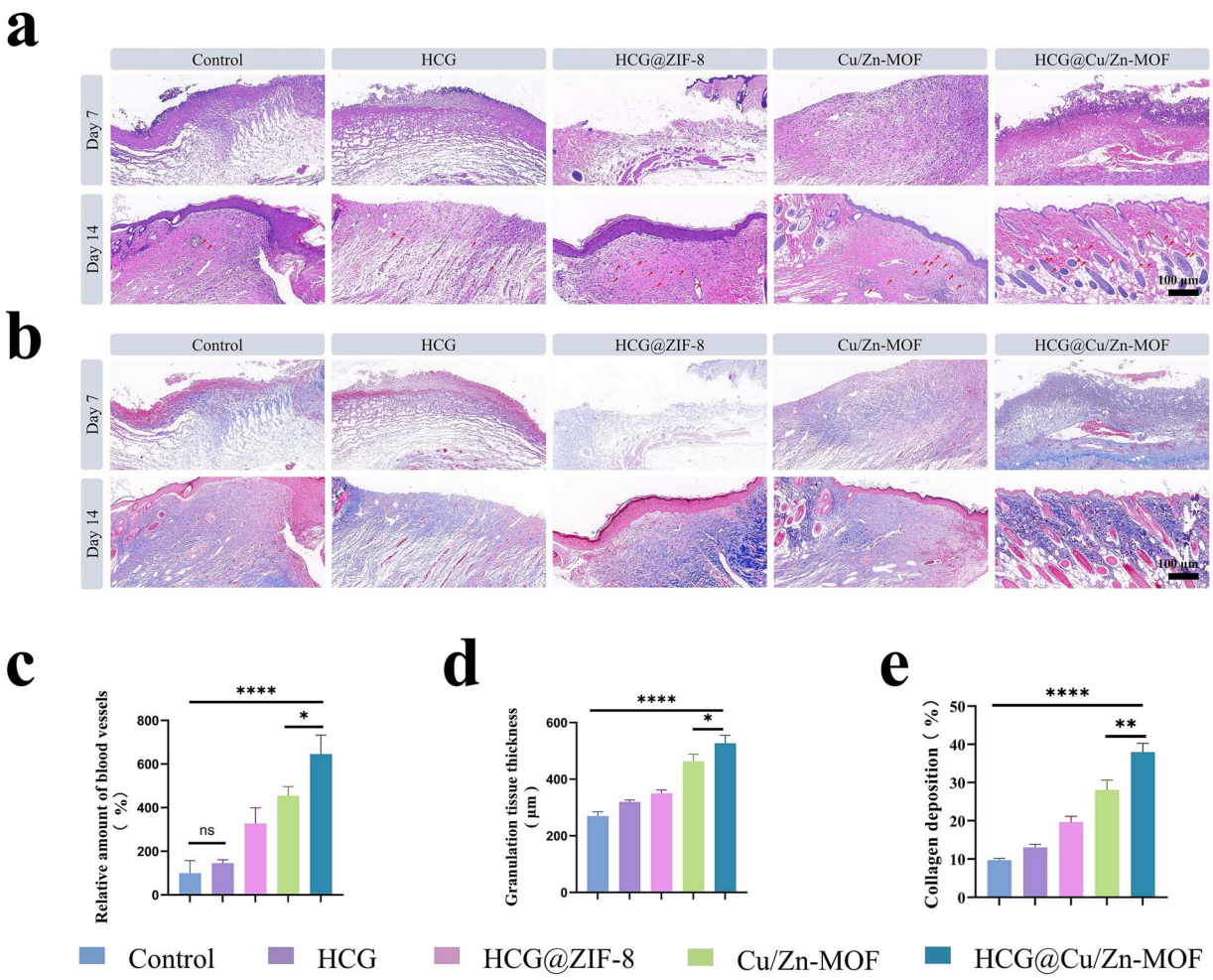


Figure 15. Histological evaluation of infected-wound tissues at different time points. (a and b) Hematoxylin and eosin and Masson's trichrome staining of infected-wound tissues on days 7 and 14. Scale bar: 100 μm. (c–e) Quantitative analysis of neovascularization, granulation tissue thickness, and collagen deposition in infected wounds ($n = 3$). All data are presented as mean ± SD. *ns* not significant; $^{*}P < 0.05$; $^{**}P < 0.01$; $^{***}P < 0.001$; $^{****}P < 0.0001$. Statistically significant differences in the experimental data were determined by performing one-way ANOVA and Tukey's post hoc test. *SD* standard deviation, *ANOVA* analysis of variance

hematological and biochemical analyses were performed at the end of treatment, and major organs from each group were collected for H&E staining. With the rapid healing of wounds treated with HCG@Cu/Zn-MOF gel, the mice showed significant increases in body weight (Figure S12, see online supplementary material). All key hematological and biochemical parameters remained within normal ranges, showing no appreciable differences compared with the control group (Figure S13, see online supplementary material). H&E staining of major organs (heart, liver, spleen, lungs, and kidneys) revealed intact tissue architecture without morphological abnormalities or inflammatory responses (Figure S14, see online supplementary material), confirming the favorable *in vivo* biocompatibility of the HCG@Cu/Zn-MOF hydrogel.

Collectively, these results demonstrate that the HCG@Cu/Zn-MOF hydrogel possesses ROS-scavenging, antimicrobial, and pro-angiogenic activities *in vivo*, as well as excellent biocompatibility, thereby accelerating diabetic wound repair.

Discussion

The treatment of diabetic wounds remains a significant clinical challenge, primarily due to persistent oxidative stress and bacterial infections. Elevated ROS disrupt cellular homeostasis, prolong inflammation, and impair tissue regeneration [53, 54]. To address these challenges, a multifunctional, temperature-sensitive hydrogel platform (HCG@Cu/Zn-MOF) was developed to reduce ROS levels, modulate the wound microenvironment, and promote healing through the synergistic effects of multi-enzyme-like activities and antimicrobial properties.

Bacterial infection and excessive ROS accumulation trigger overproduction of inflammatory factors, maintaining wounds in a chronic inflammatory state. This impairs cellular migration and angiogenesis, while excessive ROS also cause mitochondrial damage, reduce mitochondrial membrane potential, and exacerbate apoptosis [55–57]. The HCG@Cu/Zn-MOF hydrogel exhibits four peroxidase-mimicking activities, SOD, GPx, TPx, and APx, enabling the efficient decomposition of O_2^- and H_2O_2. These activities arise from the reversible redox cycling of Cu^+/Cu^{2+} ions. Specifically, Cu^+ reduces H_2O_2 via a Fenton-like reaction, generating Cu^{2+}, which is then reduced back to Cu^+ by O_2^- to yield O_2 [58]. Through this reversible cycle, Cu^+/Cu^{2+} ions continuously scavenge ROS, overcoming the major limitation of natural peroxidases, which are prone to inactivation and exhibit only short-term activity in the diabetic wound microenvironment [5].

Downloaded from academic.oup.com/burnstrauma/article/doi/10.1093/burnst/tkaf076/8341464 by guest on 12 October 2026

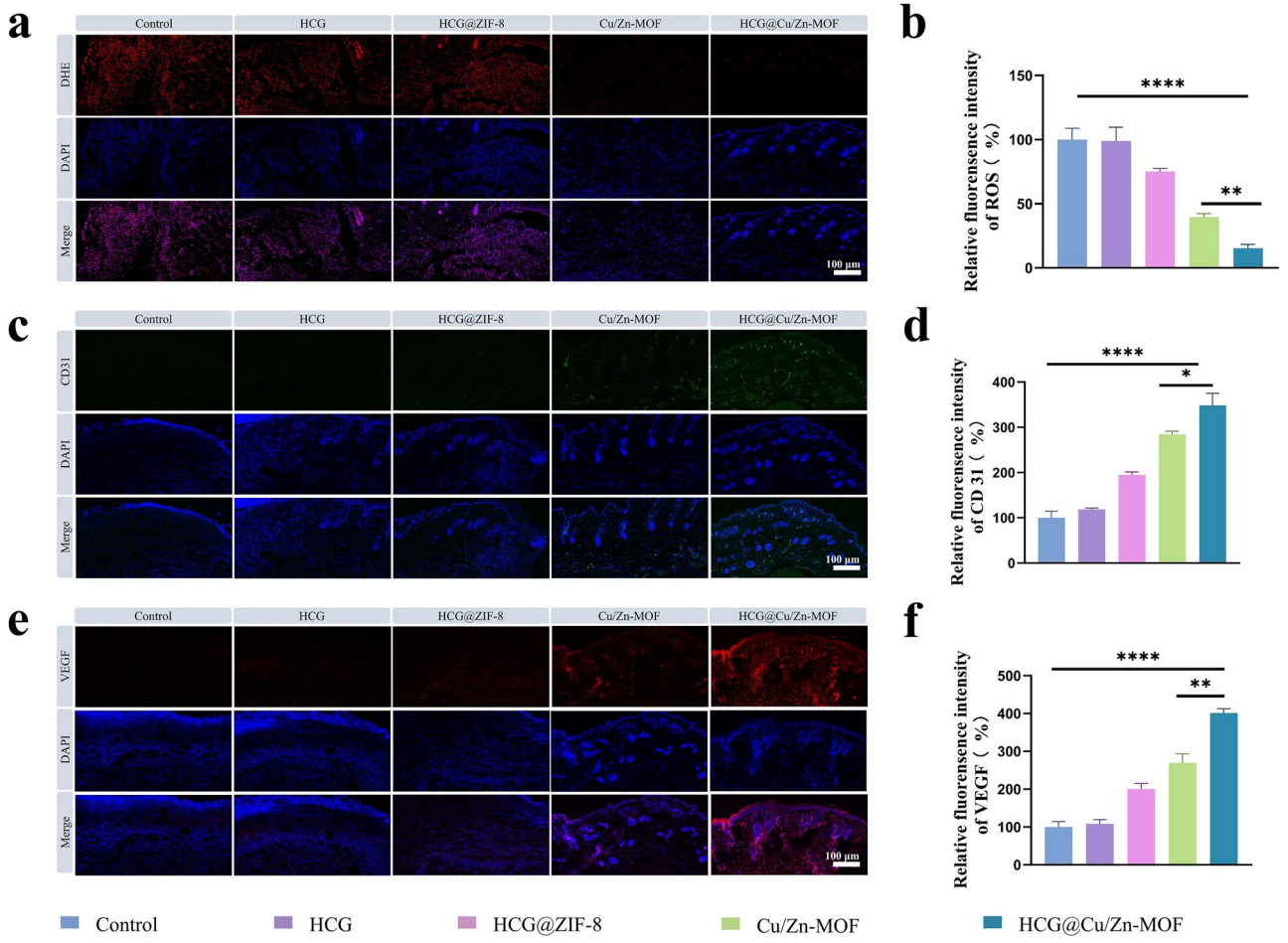


Figure 16. Pro-angiogenic and reactive oxygen species-scavenging effects of the HCG@Cu/Zn-MOF hydrogel in infected wounds. (a) Immunofluorescence staining of DHE in regenerated skin on day 14. Scale bar: 100 μm. (b) Quantitative analysis of DHE immunofluorescence (n = 3). (c) Immunofluorescence staining of CD31 in regenerated skin on day 14. Scale bar: 100 μm. (d) Quantitative analysis of CD31 immunofluorescence (n = 3). (e) Immunofluorescence staining of VEGF in regenerated skin on day 14. Scale bar: 100 μm. (f) Quantitative analysis of VEGF immunofluorescence (n = 3). All data are presented as mean ± SD. *ns* not significant; $^{*}P < 0.05$; $^{**}P < 0.01$; $^{***}P < 0.001$; $^{****}P < 0.0001$. Statistically significant differences in the experimental data were determined by performing one-way ANOVA and Tukey's post hoc test. *SD* standard deviation, MOF metal–organic framework, *HCG* hydroxypropyl methylcellulose chitosan glycerol, *ANOVA* analysis of variance, *VEGF* vascular endothelial growth factor, *DHE* dihydroethidium

Various metal-based nanoenzymes have been reported. For example, Li *et al.* [59] developed an Mn-based nanoenzyme with ROS-scavenging ability, achieving a 78.5% O_2^- scavenging rate. In the present study, the introduction of a bimetallic biomimetic site enhanced both stability and synergistic effects, achieving an even higher O_2^- scavenging rate of 88.2%. Similarly, Liu *et al.* [15] reported an ultra-small Cu-based nanoenzyme with SOD-, CAT-, and GPx-like activities that efficiently scavenged H_2O_2 at low concentrations; however, its O_2^- scavenging efficiency was limited to ~45%. Furthermore, Khivantsev *et al.* [60] proposed a method to enhance the catalytic activity of CeO_2 nanoenzymes. They demonstrated that CeO_2 nanoparticles dispersed into two-dimensional Ce_xO_y domains under a high-temperature reducing atmosphere, yielding structures with high oxygen mobility and storage capacity. This activity was further enhanced by incorporating platinum-group metals (PGMs); however, the absence of PGMs and excessive high-temperature sintering markedly reduced catalytic efficiency. In this study, Cu/Zn-MOF was synthesized via a facile method, exhibiting good stability and controlled ion release. When incorporated into HCG hydrogels, Cu/Zn-MOF provided sustained ROS-scavenging and antimicrobial effects over an extended period, thereby creating a favorable wound microenvironment.

In this study, the HCG@Cu/Zn-MOF gel suppressed NF-κB expression while scavenging ROS. Activated Sirt1 bound to the NF-κB p65 subunit and inactivated it via deacetylation, thereby downregulating pro-inflammatory factors, upregulating anti-inflammatory mediators, and interrupting the 'ROS–inflammation–ROS' cascade. Simultaneously, the gel stabilized mitochondrial membrane potential, reduced apoptosis, and enhanced the VEGF and CD31 expression, promoting angiogenesis and collagen deposition in wound tissue. Although several antioxidant hydrogels have been reported [61, 62], the present study achieved broader regulatory effects, including ROS scavenging, attenuation of inflammation, antibacterial activity, and apoptosis mitigation, thereby providing synergistic therapeutic benefits for tissue regeneration and repair.

An ideal wound dressing must be functional, broadly applicable, and highly biocompatible. Therefore, cellulose-based HPMC, approved by the U.S. Food and Drug Administration, was selected as the hydrogel matrix in this

Downloaded from academic.oup.com/burnstrauma/article/doi/10.1093/burnst/tkaf076/8341464 by guest on 12 October 2026

study. The incorporation of electrolyte salts, CS, and GLY into the HPMC solution markedly reduced the LCST. This effect may be attributed to GLY forming hydrogen bonds with water molecules, thereby reducing the hydration layer of cellulose ether. Consequently, the hydrogel undergoes a temperature-dependent physical cross-linking transition without requiring additional cross-linking agents. A sol–gel transition temperature of 37°C ensures applicability under physiological conditions while avoiding complex manipulations and the potential chemical reagent-related biotoxicity [63]. Furthermore, the excellent injectability and hydrophilicity of HCG@Cu/Zn-MOF gels enable adaptation to irregular wounds and provide a moist healing environment conducive to cell proliferation, suggesting their potential to replace traditional dressings. Moreover, their 3D porous structure enables loading of additional bioactive substances, such as stem cells or exosomes, highlighting their potential in drug-delivery applications.

Some study limitations should be considered when interpreting our findings. Although the anti-inflammatory mechanism of HCG@Cu/Zn-MOF gel has been preliminarily confirmed, transcriptomic and single-cell sequencing analyses have not yet been performed. Other potential mechanisms also must be elucidated, and the use of agonists and inhibitors to further validate mechanistic accuracy will be a focus of future studies. Furthermore, the transition to the use of hydrogel-loaded nanoenzymes in clinics faces several challenges, including establishing long-term biosafety, large-scale manufacturability, and mechanical incompatibility with human tissues, along with assessing how to manage the loss of elasticity at low temperatures, reduced stability at high temperatures, limited long-term nanoenzyme stability, and uncontrolled *in vivo* degradation. Although hydrogel loading provides a slow-release reservoir that partially overcomes the intrinsic instability of nanoenzymes, long-term stability remains a critical challenge. Therefore, future research will focus on optimizing the synthesis of hydrogels and nanoenzymes to enhance stability, improve mechanical properties, and simplify production procedures suitable for scalable manufacturing. Expanded animal studies and long-term evaluations also will be undertaken to improve generalizability and assess biosafety, with particular attention to nanoparticle accumulation, metabolism, and comprehensive toxicological assessments.

Conclusions

In this study, a novel injectable, temperature-sensitive HCG@Cu/Zn-MOF hydrogel was developed and demonstrated to accelerate wound healing in diabetic mouse models. The incorporated Cu/Zn-MOF nanoparticles exhibited multi-enzyme-like activities, enabling cascaded ROS scavenging to protect cells from oxidative stress, while also providing potent antimicrobial activity and stimulating both cell proliferation and angiogenesis. Consequently, the HCG@Cu/Zn-MOF hydrogel effectively accelerated diabetic wound repair. Histological analyses further confirmed enhanced collagen deposition and angiogenesis, accompanied by reduced inflammatory responses and ROS levels. Overall, the HCG@Cu/Zn-MOF hydrogel is a novel therapeutic strategy for chronic-wound management that holds significant promise for the treatment of diabetic wounds.

Author contributions

Wenxuan Fan (Formal analysis [equal], Investigation [equal], Methodology [equal], Supervision [equal], Writing—original draft [equal]), Ji Cheng (Formal analysis [equal], Visualization [equal], Writing—original draft [equal]), Yonghai Wang (Visualization [equal]), Hanjing Lu (Software [equal], Visualization [equal]), Jinghua Li (Project administration [equal], Writing—review & editing [equal]), Shaowen Cheng (Project administration [equal], Writing—review & editing [equal])

Supplementary data

Supplementary data is available at *Burns & Trauma* online.

Ethics approval and consent to participate

All animal experiments were approved by the Ethics Committee of Hainan Medical University.

Conflict of interest

The authors declare no competing interests.

Funding

This study was supported by the Hainan Province Clinical Medical Center and the Innovation Platform for Academicians of Hainan Province, the Hainan Provincial Natural Science Foundation (822MS174, 823MS045), the Hainan Province Science and Technology Special Fund (ZDYF2025SHFZ049, ZDKJ2021038), the National Natural Science Foundation of China (82260373, 82560446), the National Natural Science Foundation of China (32260237), the Hainan Provincial Natural Science Foundation Youth Fund Project (825QN318), the Hainan Province Higher Education Teaching Reform Research Project (Hnjg2024ZD-36), the Science and Technology Plan Project of Qinghai Province Incentive Fund 2024, the Open Fund of the Key Laboratory of Green and High-end Utilization of Salt Lake Resources (ISL2024-01), the Second Tibetan Plateau Scientific Expedition and Research Program (2019QZKK0805-02), and the Innovative Postgraduate Projects of Hainan Medical University (Qhys2023-420).

Data availability

The data supporting the findings of this study are available from the corresponding authors upon reasonable request.

References

1. Cheng S, Wang H, Pan X, Zhang C, Zhang K, Chen Z, *et al.* Dendritic hydrogels with robust inherent antibacterial properties for promoting bacteria-infected wound healing. *ACS Appl Mater Interfaces* 2022;**14**:11144–55. https://doi.org/10.1021/acsami.1c25014.
2. Cai Y, Chen K, Liu C, Qu X. Harnessing strategies for enhancing diabetic wound healing from the perspective of spatial inflammation patterns. *Bioact Mater* 2023;**28**:243–54. https://doi.org/10.1016/j.bioactmat.2023.04.019.
3. Saeedi P, Petersohn I, Salpea P, Malanda B, Karuranga S, Unwin N, *et al.* Global and regional diabetes prevalence estimates for 2019 and projections for 2030 and 2045: results from the international diabetes federation diabetes atlas, 9th edition. *Diabetes Res Clin Pract* 2019;**157**:107843. https://doi.org/10.1016/j.diabres.2019.107843.
4. Cho H, Blatchley MR, Duh EJ, Gerecht S. Acellular and cellular approaches to improve diabetic wound healing. *Adv Drug Deliv Rev* 2019;**146**:267–88. https://doi.org/10.1016/j.addr.2018.07.019.

Downloaded from academic.oup.com/burnstrauma/article/doi/10.1093/burnst/tkaf076/8341464 by guest on 12 October 2026

5. Deng L, Du C, Song P, Chen T, Rui S, Armstrong DG, *et al.* The role of oxidative stress and antioxidants in diabetic wound healing. *Oxidative Med Cell Longev* 2021;**2021**:8852759. https://doi.org/10.1155/2021/8852759.
6. Yuan T, Yang T, Chen H, Fu D, Hu Y, Wang J, *et al.* New insights into oxidative stress and inflammation during diabetes mellitus-accelerated atherosclerosis. *Redox Biol* 2019;**20**:247–60. https://doi.org/10.1016/j.redox.2018.09.025.
7. Zhao X, Wang LY, Li JM, Peng LM, Tang CY, Zha XJ, *et al.* Redox-mediated artificial non-enzymatic antioxidant MXene nanoplatforms for acute kidney injury alleviation. *Adv Sci* 2021;**8**:e2101498. https://doi.org/10.1002/advs.202101498.
8. Rizwan H, Pal S, Sabnam S, Pal A. High glucose augments ROS generation regulates mitochondrial dysfunction and apoptosis via stress signalling cascades in keratinocytes. *Life Sci* 2020;**241**:117148. https://doi.org/10.1016/j.lfs.2019.117148.
9. Sabnam S, Rizwan H, Pal S, Pal A. CEES-induced ROS accumulation regulates mitochondrial complications and inflammatory response in keratinocytes. *Chem Biol Interact* 2020;**321**:109031. https://doi.org/10.1016/j.cbi.2020.109031.
10. Fu J, Chen X, Liu X, Xu D, Yang H, Zeng C, *et al.* ELABELA ameliorates hypoxic/ischemic-induced bone mesenchymal stem cell apoptosis via alleviation of mitochondrial dysfunction and activation of PI3K/AKT and ERK1/2 pathways. *Stem Cell Res Ther* 2020;**11**:541. https://doi.org/10.1186/s13287-020-02063-1.
11. Morse PT, Arroum T, Wan J, Pham L, Vaishnav A, Bell J, *et al.* Phosphorylations and Acetylations of Cytochrome c Control Mitochondrial Respiration, Mitochondrial Membrane Potential, Energy, ROS, and Apoptosis. *Cells*. 2024;**13**:493. https://doi.org/10.3390/cells13060493.
12. Li F, Zhang C, Zhong X, Li B, Zhang M, Li W, *et al.* A 3D radially aligned nanofiber scaffold co-loaded with LL37 mimetic peptide and PDGF-BB for the management of infected chronic wounds. *Mater Today Bio*. 2024;**28**:101237. https://doi.org/10.1016/j.mtbio.2024.101237.
13. Holl J, Kowalewski C, Zimek Z, Fiedor P, Kaminski A, Oldak T, *et al.* Chronic Diabetic Wounds and Their Treatment with Skin Substitutes. *Cells*. 2021;**10**:655. https://doi.org/10.3390/cells10030655.
14. Xu Z, Liu Y, Ma R, Chen J, Qiu J, Du S, *et al.* Thermosensitive hydrogel incorporating Prussian blue nanoparticles promotes diabetic wound healing via ROS scavenging and mitochondrial function restoration. *ACS Appl Mater Interfaces* 2022;**14**:14059–71. https://doi.org/10.1021/acsami.1c24569.
15. Liu T, Xiao B, Xiang F, Tan J, Chen Z, Zhang X, *et al.* Ultrasmall copper-based nanoparticles for reactive oxygen species scavenging and alleviation of inflammation related diseases. *Nat Commun* 2020;**11**:2788. https://doi.org/10.1038/s41467-020-16544-7.
16. Zhang C, Wang X, Du J, Gu Z, Zhao Y. Reactive oxygen species-regulating strategies based on nanomaterials for disease treatment. *Adv Sci* 2020;**8**:2002797. https://doi.org/10.1002/advs.202002797.
17. Nguyen NH, Tran GB, Nguyen CT. Anti-oxidative effects of superoxide dismutase 3 on inflammatory diseases. *J Mol Med* 2020;**98**:59–69. https://doi.org/10.1007/s00109-019-01845-2.
18. Kumar S, Bhardwaj VK, Guleria S, Purohit R, Kumar S. Improving the catalytic efficiency and dimeric stability of Cu, Zn superoxide dismutase by combining structure-guided consensus approach with site-directed mutagenesis. *Biochim Biophys Acta Bioenerg* 2022;**1863**:148505. https://doi.org/10.1016/j.bbabio.2021.148505.
19. Shang L, Yu Y, Jiang Y, Liu X, Sui N, Yang D, *et al.* Ultrasound-augmented multienzyme-like nanozyme hydrogel spray for promoting diabetic wound healing. *ACS Nano* 2023;**17**:15962–77. https://doi.org/10.1021/acsnano.3c04134.
20. Lu X, Gao S, Lin H, Tian H, Xu D, Shi J. Bridging oxidase catalysis and oxygen reduction electrocatalysis by model single-atom catalysts. *Natl Sci Rev* 2022;**9**:nwac022. https://doi.org/10.1093/nsr/nwac022.
21. Mu J, Li C, Shi Y, Liu G, Zou J, Zhang DY, *et al.* Protective effect of platinum nano-antioxidant and nitric oxide against hepatic ischemia-reperfusion injury. *Nat Commun* 2022;**13**:2513. https://doi.org/10.1038/s41467-022-29772-w.
22. Jiang B, Guo Z, Liang M. Recent progress in single-atom nanozymes research. *Nano Res* 2023;**16**:1878–89. https://doi.org/10.1007/s12274-022-4856-7.
23. Singh R, Umapathi A, Patel G, Patra C, Malik U, Bhargava SK, *et al.* Nanozyme-based pollutant sensing and environmental treatment: trends, challenges, and perspectives. *Sci Total Environ* 2023;**854**:158771. https://doi.org/10.1016/j.scitotenv.2022.158771.
24. Jin G-X, Liu J, Wang C, Gu W-X, Ran G-X, Liu B, *et al.* Ir nanoparticles with multi-enzyme activities and its application in the selective oxidation of aromatic alcohols. *Appl Catal B Environ* 2020;**267**:118725. https://doi.org/10.1016/j.apcatb.2020.118725.
25. Yang D, Chen Z, Gao Z, Tammina SK, Yang Y. Nanozymes used for antimicrobials and their applications. *Colloids Surf B Biointerfaces* 2020;**195**:111252. https://doi.org/10.1016/j.colsurfb.2020.111252.
26. Liu X, Huang D, Lai C, Qin L, Zeng G, Xu P, *et al.* Peroxidase-like activity of smart nanomaterials and their advanced application in colorimetric glucose biosensors. *Small* 2019;**15**:e1900133. https://doi.org/10.1002/smll.201900133.
27. Chen Z, Yu Y, Gao Y, Zhu Z. Rational design strategies for nanozymes. *ACS Nano* 2023;**17**:13062–80. https://doi.org/10.1021/acsnano.3c04378.
28. Ali A, Ovais M, Zhou H, Rui Y, Chen C. Tailoring metal–organic frameworks-based nanozymes for bacterial theranostics. *Biomaterials* 2021;**275**:120951. https://doi.org/10.1016/j.biomaterials.2021.120951.
29. Li Q-J, Xing F, Wu W-T, Zhe M, Zhang W-Q, Qin L, *et al.* Multifunctional metal–organic frameworks as promising nanomaterials for antimicrobial strategies. *Burns Trauma* 2025;**13**:tkaf008. https://doi.org/10.1093/burnst/tkaf008.
30. Wang J, Zhou Y, Zeng M, Zhao Y, Zuo X, Meng F, *et al.* Zr(IV)-based metal-organic framework nanocomposites with enhanced peroxidase-like activity as a colorimetric sensing platform for sensitive detection of hydrogen peroxide and phenol. *Environ Res* 2022;**203**:111818. https://doi.org/10.1016/j.envres.2021.111818.
31. Dong W, Yang L, Huang Y. Glycine post-synthetic modification of MIL-53(Fe) metal-organic framework with enhanced and stable peroxidase-like activity for sensitive glucose biosensing. *Talanta* 2017;**167**:359–66. https://doi.org/10.1016/j.talanta.2017.02.039.
32. Li S, Liang L, Tian L, Wu J, Zhu Y, Qin Y, *et al.* Enhanced peroxidase-like activity of MOF nanozymes by co-catalysis for colorimetric detection of cholesterol. *J Mater Chem B* 2023;**11**:7913–9. https://doi.org/10.1039/D3TB00958K.
33. Wang J, Bao M, Wei T, Wang Z, Dai Z. Bimetallic metal-organic framework for enzyme immobilization by biomimetic mineralization: constructing a mimic enzyme and simultaneously immobilizing natural enzymes. *Anal Chim Acta* 2020;**1098**:148–54. https://doi.org/10.1016/j.aca.2019.11.039.
34. Maleki A, He J, Bochani S, Nosrati V, Shahbazi MA, Guo B. Multifunctional photoactive hydrogels for wound healing acceleration. *ACS Nano* 2021;**15**:18895–930. https://doi.org/10.1021/acsnano.1c08334.
35. Wang Y, Wu H, Pan Y, Xiao Y, Chen Y, Yang S, *et al.* Innovations in hydrogel therapies for diabetic wound healing: bridging the gap between pathophysiology and clinical application. *Burns Trauma* 2025;**13**:tkaf025. https://doi.org/10.1093/burnst/tkaf025.
36. Klouda L. Thermoresponsive hydrogels in biomedical applications: a seven-year update. *Eur J Pharm Biopharm* 2015;**97**:338–49. https://doi.org/10.1016/j.ejpb.2015.05.017.

Downloaded from academic.oup.com/burnstrauma/article/doi/10.1093/burnst/tkaf076/8341464 by guest on 12 October 2026

37. Alven S, Aderibigbe BA. Chitosan and cellulose-based hydrogels for wound management. *Int J Mol Sci* 2020;**21**:9656. https://doi.org/10.3390/ijms21249656.
38. Kim MH, Park H, Nam HC, Park SR, Jung JY, Park WH. Injectable methylcellulose hydrogel containing silver oxide nanoparticles for burn wound healing. *Carbohydr Polym* 2018;**181**:579–86. https://doi.org/10.1016/j.carbpol.2017.11.109.
39. Xu L, Jiao G, Huang Y, Ren P, Liang M, Wei D, *et al.* Laponite nanoparticle-crosslinked carboxymethyl cellulose-based injectable hydrogels with efficient underwater-specific adhesion for rapid hemostasis. *Int J Biol Macromol* 2024;**255**:128288. https://doi.org/10.1016/j.ijbiomac.2023.128288.
40. Perez-Robles S, Carotenuto C, Minale M. HPMC hydrogel formation mechanisms unveiled by the evaluation of the activation energy. *Polymers* 2022;**14**:635. https://doi.org/10.3390/polym14030635.
41. Wang L, Song D, Wei C, Chen C, Yang Y, Deng X, *et al.* Telocytes inhibited inflammatory factor expression and enhanced cell migration in LPS-induced skin wound healing models *in vitro* and *in vivo*. *J Transl Med* 2020;**18**:60. https://doi.org/10.1186/s12967-020-02217-y.
42. Amanzholkyzy A, Zhumagaliyeva S, Sultanova N, Abilov Z, Ongalbek D, Donbayeva E, *et al.* Hydrogel delivery systems for biological active substances: properties and the role of HPMC as a carrier. *Molecules* 2025;**30**:1354. https://doi.org/10.3390/molecules30061354.
43. An Y, Xu B-T, Wan S-R, Ma X-M, Long Y, Xu Y, *et al.* The role of oxidative stress in diabetes mellitus-induced vascular endothelial dysfunction. *Cardiovasc Diabetol* 2023;**22**:237. https://doi.org/10.1186/s12933-023-01965-7.
44. Kang T, Kim YG, Kim D, Hyeon T. Inorganic nanoparticles with enzyme-mimetic activities for biomedical applications. *Coord Chem Rev* 2020;**403**:213092. https://doi.org/10.1016/j.ccr.2019.213092.
45. Liu Y, Cheng Y, Zhang H, Zhou M, Yu Y, Lin S, *et al.* Integrated cascade nanozyme catalyzes *in vivo* ROS scavenging for anti-inflammatory therapy. *Sci Adv* 2020;**6**:eabb2695. https://doi.org/10.1126/sciadv.abb2695.
46. Liu W, Zhang Y, Wei G, Zhang M, Li T, Liu Q, *et al.* Integrated cascade nanozymes with antisenescence activities for atherosclerosis therapy. *Angew Chem Int Ed Engl* 2023;**62**:e202304465. https://doi.org/10.1002/anie.202304465.
47. Caligiuri G. CD31 as a therapeutic target in atherosclerosis. *Circ Res* 2020;**126**:1178–89. https://doi.org/10.1161/CIRCRESAHA.120.315935.
48. Peña OA, Martin P. Cellular and molecular mechanisms of skin wound healing. *Nat Rev Mol Cell Biol* 2024;**25**:599–616. https://doi.org/10.1038/s41580-024-00715-1.
49. Wang R, Li B, Dong M, Zhu H, Jin P, Zou Y. Targeting oxidative damage in diabetic foot ulcers: integrative strategies involving antioxidant drugs and nanotechnologies. *Burns Trauma* 2025;**13**:tkaf020. https://doi.org/10.1093/burnst/tkaf020.
50. Anilkumar S, Wright-Jin E. NF-κB as an Inducible Regulator of Inflammation in the Central Nervous System. *Cells*. 2024;**13**:485. https://doi.org/10.3390/cells13060485.
51. Zhang P, He L, Zhang J, Mei X, Zhang Y, Tian H, *et al.* Preparation of novel berberine nano-colloids for improving wound healing of diabetic rats by acting Sirt1/NF-κB pathway. *Colloids Surf B Biointerfaces* 2020;**187**:110647. https://doi.org/10.1016/j.colsurfb.2019.110647.
52. Rousselle P, Braye F, Dayan G. Re-epithelialization of adult skin wounds: cellular mechanisms and therapeutic strategies. *Adv Drug Deliv Rev* 2019;**146**:344–65. https://doi.org/10.1016/j.addr.2018.06.019.
53. Zhang Y, Li M, Wang Y, Han F, Shen K, Luo L, *et al.* Exosome/metformin-loaded self-healing conductive hydrogel rescues microvascular dysfunction and promotes chronic diabetic wound healing by inhibiting mitochondrial fission. *Bioact Mater* 2023;**26**:323–36. https://doi.org/10.1016/j.bioactmat.2023.01.020.
54. Qi X, Cai E, Xiang Y, Zhang C, Ge X, Wang J, *et al.* An immunomodulatory hydrogel by hyperthermia-assisted self-cascade glucose depletion and ROS scavenging for diabetic foot ulcer wound therapeutics. *Adv Mater* 2023;**35**:e2306632. https://doi.org/10.1002/adma.202306632.
55. Vasileiou PVS, Evangelou K, Vlasis K, Fildisis G, Panayiotidis MI, Chronopoulos E, *et al.* Mitochondrial homeostasis and cellular senescence. *Cells* 2019;**8**:686. https://doi.org/10.3390/cells8070686.
56. De Gaetano A, Gibellini L, Zanini G, Nasi M, Cossarizza A, Pinti M. Mitophagy and oxidative stress: the role of aging. *Antioxidants* 2021;**10**:794. https://doi.org/10.3390/antiox10050794.
57. Boardman NT, Trani G, Scalabrin M, Romanello V, Wüst RCI. Intracellular to interorgan mitochondrial communication in striated muscle in health and disease. *Endocr Rev* 2023;**44**:668–92. https://doi.org/10.1210/endrev/bnad004.
58. Ge H, Wang M, Wei X, Chen XL, Wang X. Copper-based nanozymes: potential therapies for infectious wounds. *Small* 2025;**21**:e2407195. https://doi.org/10.1002/smll.202407195.
59. Li X, Liu Y, Qi X, Xiao S, Xu Z, Yuan Z, *et al.* Sensitive activatable nanoprobes for real-time ratiometric magnetic resonance imaging of reactive oxygen species and ameliorating inflammation *in vivo*. *Adv Mater* 2022;**34**:e2109004. https://doi.org/10.1002/adma.202109004.
60. Khivantsev K, Pham H, Engelhard MH, Aleksandrov HA, Kovarik L, Bowden M, *et al.* Transforming ceria into 2D clusters enhances catalytic activity. *Nature* 2025;**640**:947–53. https://doi.org/10.1038/s41586-025-08684-x.
61. Andrabi SM, Majumder S, Gupta KC, Kumar A. Dextran based amphiphilic nano-hybrid hydrogel system incorporated with curcumin and cerium oxide nanoparticles for wound healing. *Colloids Surf B Biointerfaces* 2020;**195**:111263. https://doi.org/10.1016/j.colsurfb.2020.111263.
62. Xia Y, Li X, Huang F, Wu Y, Liu J, Liu J. Design and advances in antioxidant hydrogels for ROS-induced oxidative disease. *Acta Biomater* 2025;**194**:80–97. https://doi.org/10.1016/j.actbio.2025.01.057.
63. Ye J, Xiao Z, Gao L, Zhang J, He L, Zhang H, *et al.* Assessment of the effects of four crosslinking agents on gelatin hydrogel for myocardial tissue engineering applications. *Biomed Mater* 2021;**16**:045026. https://doi.org/10.1088/1748-605X/abfff2.

Downloaded from academic.oup.com/burnstrauma/article/doi/10.1093/burnst/tkaf076/8341464 by guest on 12 October 2026

© The Author(s) 2025. Published by Oxford University Press. This is an Open Access article distributed under the terms of the Creative Commons Attribution-NonCommercial License (https://creativecommons.org/licenses/by-nc/4.0/), which permits non-commercial re-use, distribution, and reproduction in any medium, provided the original work is properly cited. For commercial re-use, please contact reprints@oup.com for reprints and translation rights for reprints. All other permissions can be obtained through our RightsLink service via the Permissions link on the article page on our site—for further information please contact journals.permissions@oup.com.
Burns & Trauma, 2026, 14, tkaf076
https://doi.org/10.1093/burnst/tkaf076
Research Article